AD-A157 533 INTERMEDIATE AND HIGH-FREQUENCY ACOUSTIC BACKSCATTERING 1/1
CROSS SECTIONS FO.. (U) MIDDLETON (DAVID) NEW YORK
D MIDDLETON 07 MAR 85 NUSC-TD-7375 N00140-83-M-PL78
UNCLASSIFIED F/G 20/1 NL

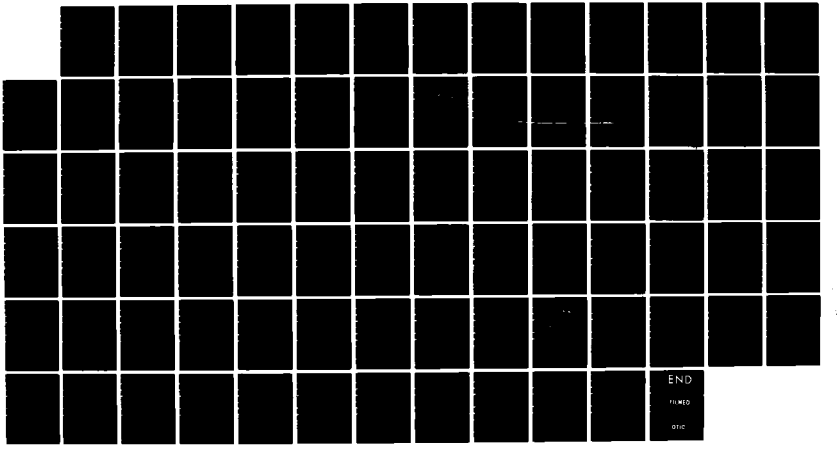

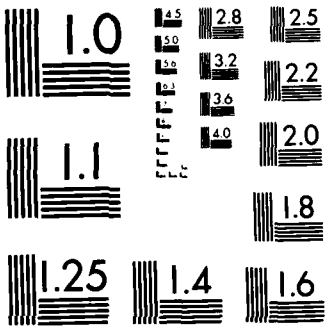

MICROCOPY RESOLUTION TEST CHART

(2)

NUSC Technical Document 7375
7 March 1985

Intermediate and High-Frequency Acoustic Backscattering Cross Sections for Water-Ice Interfaces: I. Two-Component Profile Models

David Middleton
(Consultant)

Associate Technical Director
for Technology

Naval Underwater Systems Center
Newport, Rhode Island/New London, Connecticut

Preface

This work was accomplished under NUSC's Arctic Program, Code 01Y and Code 10. The sponsoring activity is the Naval Underwater Systems Center, Earle Messere, Director. This document was prepared for the Research and Technology Staff by David Middleton, 127 E. 91 Street, New York, NY 10128.

Acknowledgments

The author wishes particularly to thank Drs. Peter Cable and Frederick DiNapoli for many fruitful discussions in the course of this research.

Reviewed and Approved: 19 April 1985

W. A. Von Winkle
Associate Technical Director for Technology

Unclassified

REPORT DOCUMENTATION PAGE

READ INSTRUCTIONS BEFORE COMPLETING FORM

1. REPORT NUMBER: NUSC TD 7375	2. GOVT ACCESSION NO.: AD-A157 553
3. RECIPIENT'S CATALOG NUMBER:	
4. TITLE (and Subtitle): Intermediate and High-Frequency Acoustic Back-scattering Cross Sections for Water-Ice Interfaces: I. Two-Component Profile Models	5. TYPE OF REPORT & PERIOD COVERED: Technical Report Aug., 1983-Nov. 30, 1984
	6. PERFORMING ORG. REPORT NUMBER:
7. AUTHOR(s): David Middleton	8. CONTRACT OR GRANT NUMBER(s): N00140-83-M-PL78 N00140-84-M-MS42
9. PERFORMING ORGANIZATION NAME AND ADDRESS: Dr. David Middleton 127 E. 91 St. New York, NY 10128	10. PROGRAM ELEMENT, PROJECT, TASK AREA & WORK UNIT NUMBERS:
11. CONTROLLING OFFICE NAME AND ADDRESS: Naval Underwater Systems Center, Code 01Y New London, Conn. 06320	12. REPORT DATE: 7 March 1985
	13. NUMBER OF PAGES: 69 + ix
14. MONITORING AGENCY NAME & ADDRESS (if different from Controlling Office):	15. SECURITY CLASS. (of this report): Unclassified
	15a. DECLASSIFICATION/DOWNGRADING SCHEDULE:

16. DISTRIBUTION STATEMENT (of this Report)

Approved for public release; distribution unlimited

17. DISTRIBUTION STATEMENT (of the abstract entered in Block 20, if different from Report)

18. SUPPLEMENTARY NOTES

19. KEY WORDS (Continue on reverse side if necessary and identify by block number)

Underwater acoustic scattering; underice scattering; scattering cross sections; underice profile; numerical examples; two-component surfaces; scattering models; intermediate, high frequencies, backscatter intensities for small angles.

20. ABSTRACT (Continue on reverse side if necessary and identify by block number)

Two general statistical-physical models (I, II) for underice surface elevations ζ are constructed. These provide the basis for determining the intensities and associated frequency spectra of acoustic waves scattered from such water-ice interfaces. Both models embody two-component processes: the simpler model (I) represents the interface as an appropriately weighted sum of two gaussian distributions of elevation ζ, each with different non-zero means and variances. No explicit identification of keel structure is made,

DD FORM 1 JAN 73 1473 EDITION OF 1 NOV 65 IS OBSOLETE

S/N 0102-LF-014-6601

Unclassified

however. The second model (II) does account for keel structure and assigns the gaussian components of the first model respectively to two distinct physical processes: that of local ice generation ~~(process S)~~, of ζ_S, and that of the intermittent, large-scale keel formation, [process K and elevation ζ_K]. Two variants of II are also distinguished here.

The empirical basis for these models is the underice historgram of Lyon [1], [2], which can be interpreted to support the concept of a distinct keel structure (Model II), although the precise existence of the latter is subject to some dispute [3]. On physical grounds it appears reasonable to treat the formation of the comparatively small- and large-scale ice structures as separate physical processes, each the resultant of many effectively independent forces, so that gaussian elevations follow (at least approximately), as indicated by the Lyon data.

In this Report the analysis is limited to Model I and calculations of backscattering cross sections appropriate to intermediate and high frequencies ~~(~~$O(\geq 0.1$ kHz), i.e., Kirchoff-based methods. The treatment here is also restricted, for the moment, to zero gradient ~~($\nabla\zeta=0$)~~ and single ice bottom surface interactions. In most instances, the Rayleigh numbers for both components of the underice surface are large, so that theories based solely on perturbation techniques and/or Bragg scatter are inadequate.

The construction of second-order characteristic functions (c.f.'s) of the underice profile ζ is accordingly required. The second-order c.f. is modeled here by a single gauss process, whose first-order moments are those determined from the two-component, first-order gauss process fitted to the Lyon data. Because of the large Rayleigh numbers involved, an (artificial) splitting of the surface wave number spectrum must be made, to separate the "rough" (i.e., Kirchoff) components from the Bragg (i.e., "smooth") components of the scattering surfaces. The analytic methods and results used here are direct modifications of the author's recent studies of scattering from moving ocean wave surfaces [4]. The present treatment is directly applicable to intermediate $O(\geq 100$ Hz) and high frequencies $O(> 1.0$ kHz).

In addition to the analytic results for scattering cross sections developed here for Model I, it is found that the simple, single surface version (Model Ia) is inadequate to account for the (much) larger empirical (back-)scatter cross sections observed, particularly at small grazing angles ($\phi = 10°$) and high frequencies ($f_0 = 1$ kHz). Accordingly, a two-component version (Model Ib) is proposed, where now an additional, independent surface projection rides on the single surface of Model Ia. RMS elevations $O(\sigma_k = 8\text{-}15$ cm) and correlation distances $O(\ell_c = 4\text{-}7$ cm) for this second surface component are required for reasonable agreement with the data cited [5], [24]. It is emphasized that, at the present stage of limited available data, it is the choice of parameter values, rather than any specific analytic model form, which is critical to the potential applicability of the model in question.

The results developed here also indicate the need for: (1), profile elevation statistics with a much finer resolution than presently available, say $O(\lambda_0 = 6$ m - 1 cm), with particular emphasis on the range O(20 cm - 1 cm); (2), (rms) slopes and slope statistics; (3), directional data on profile elevations; and (4), scattering results for Model II, both for those cases where a definite keel structure exists, and for comparison with Models Ia,b as generated here.

TABLE OF CONTENTS

LIST OF ILLUSTRATIONS

LIST OF PRINCIPAL SYMBOLS

A = beam parameter

A_1 = beam area in illuminated surface

α_{ox}, α_{oy}, α_{oz}; $\underset{\sim}{\alpha}_{o\perp}$ = scattering angles

B = beam parameter

$b_o = \cos\theta_{oT} + \cos\theta_{oR}$

C_1 = spectrum parameter

c_I, c_W = speed of sound in ice, water

δ, δ_k = unit functions on a finite region

$\underset{\sim}{\delta}$ = (2-dimensional) delta function

δ= delta function

F_1, F_2 = characteristic functions

f_c = (carrier) frequency of sound source

f_D = spectrum splitting frequency

γ_o = density of "bumps" (ice projections) per unit surface area

$I^{(0)}$, $I^{(2)}$, $I^{(4)}$ = tilt integrals

$\hat{\underset{\sim}{i}}$, $\hat{\underset{\sim}{i}}_x$, $\hat{\underset{\sim}{i}}_y$, $\hat{\underset{\sim}{i}}_z$, $\hat{\underset{\sim}{i}}_T$, $\hat{\underset{\sim}{i}}_R$ = unit vectors

J_o = Bessel function of first kind

K_ζ, K_h = surface covariances

K_1, K_2 = modified Bessel functions of second kind

k_c = spectrum wave number parameter

k_o, k, $\underset{\sim}{k}$ = wave numbers

L_o = "bump" length

ℓ_c = correlation distance

ℓ_h = "bump" length

Λ, Λ_K = regions on a plane

λ_o = source wavelength

λ_D = spectrum splitting wavelength

m_S, m_K = mean values

$N_{LH}^{(0)}$, $\hat{N}_{LH}^{(0)}$, $N_{Lh}^{(0)}$ = "tilt-factors"

$\hat{\underset{\sim}{n}}_K$, $\hat{\underset{\sim}{n}}_L$, $\hat{\underset{\sim}{n}}_S$ = unit normals to a surface (K,L,S)

$\langle \phi_L^2 \rangle^{\frac{1}{2}}$ = rms ice slope angle

pdf = probability density function

ϕ_{oT} = horizontal angle

R_o = (plane-) wave reflection coefficient

R, R_H, R_ζ = rayleigh number

$\underset{\sim}{r}_1$, r, $\underset{\sim}{\Delta r}$, Δr = distances

ρ, ρ_h, ρ_ζ, ρ_S, ρ_K = normalized covariances

ρ_c = radius of curvature

$\mathcal{S}$ = shadowing function

$\partial^{(0)}$ = scattering cross section

$\sigma_{L(x=y)}$ = rms slopes

σ_ρ, σ_S, σ_K, σ_h, σ_H = rms elevations

$\mathcal{S}_\zeta$ = amplitude spectral density

θ_{oT} = vertical angle

W_H, W_h, W_1, W_2 = wave number intensity spectra

w_1 = first-order pdf

ζ, ζ_h, ζ_K, ζ_S, ζ_L, ζ_H = profile elevations, components

ζ_x, ζ_y, ζ_{Lx}, ζ_{Ly} = profile slopes

ζ_o = "bump" elevation

INTERMEDIATE AND HIGH-FREQUENCY ACOUSTIC BACKSCATTERING CROSS SECTIONS FOR WATER-ICE INTERFACES: I. TWO-COMPONENT PROFILE MODELS*

by

David Middleton**

I. Introduction

The purpose of this study is twofold: (1), to develop several plausible statistical-physical models of typical underice "profiles"† of elevations, ζ, which can then be used (2), to obtain acoustic scattering intensities and spectra. Here we shall describe two general models of underice elevations, and use the simpler one for an initial determination of backscatter cross sections. The extension of these results to the more complex second model is reserved to a subsequent study, for which the present investigation is prototypical. In addition here, we shall limit our analysis to zero-gradient oceans and single ice-bottom interactions. The emphasis here is on acoustic backscattering, but the methods described are directly extendable to bi-static geometries.

We base both our models on the (one-dimensional) underice profile data of Lyon [1], [2], [24]. Figure 1.1 shows these data fitted by two (first-order) gaussian probability densities for ζ. No attempt has been made in this initial fitting to apply any specific "best-fit" techniques: simple trial adjustments of means and variances, only, were used to obtain a visually reasonable fit, which can be improved upon but without major changes in the resulting parameter values.

Our first model (I, and specifically Ia here) postulates two

---

*Work supported under contract with the Naval Underwater Systems Center, New London, Conn., N00140-83-M-PL78, 1983, and in part, under Contract N00140-84-M-MS42, 1984.

**Contractor: Physics and Applied Mathematics, 127 E. 91 St., New York, NY 10128.

†We shall use the term "profile" here interchangeably with "surface elevation," which is a function of surface coordinates (x',y'), cf. Fig. (2.2a)ff., e.g., $\zeta = \zeta(\underset{\sim}{r})$.

independent surface processes combining in some fashion to produce a single surface, ζ. These two processes consist, respectively, of a comparatively small-scale [m_S = 4.5 m; σ_S = O(1 m)] elevation, ζ_S, in turn, which is accompanied by a larger-scale surface component, ζ_K, [m_K = 12.5 m; σ_K = 3.0 m]. As noted, these coëxist in some unspecified fashion geometrically, but in such a way that the distributions (and probability densities) of ζ_S and ζ_K add*, in the manner of Figure 1.1, to give the distributions (etc.) of the total profile ζ, cf. Sec. 2.1 ff. This first model (I) does not specify keel structure as such explicitly. On the other hand, our second model (II) does, by identifying the second (or larger-scale) gaussian elevation ζ_K with keel structure, on which may "ride" the smaller-scale gaussian elevation component ζ_S (Model IIb). Unlike Model I, the total elevation, or profile process ζ, is an (appropriately weighted) sum of the independent processes ζ_S and ζ_K, cf. Sec. 2.2 ff. Both these models are described analytically in Section 2 following. Because there is some doubt as to the unambiguous geometrical existence of keels [3], Model I (which is the more phenomenological of the two) may prove a useful candidate model. Decision between them will depend both on additional data and on how well the corresponding theoretical results agree with experiment.

In any case, we emphasize that both models are potentially capable of handling all frequencies (above O(30-50 Hz)) of incident acoustic radiation, as noted in Sec. 3 ff.: neither is restricted to the small Rayleigh number cases of Bragg scatter alone [5], and each can employ appropriate shadowing and reflection functions [4]. Apart from the fit to the empirical data [cf. Fig. 1.1], gaussian distributions (and hence gaussian processes ultimately) appear more reasonable than other choices. In a fundamental way we would say that the process of surface formation consists of the superposition of many independent effects, so that the usual Central Limit Theorem arguments [6] apply. Moreover, the presence

---

*Note that this is not the same thing as the distribution (and pdf) of the process sum $\zeta = a_1\zeta_S + a_2\zeta_K$, cf. Sec. 2 ff. See Appendix A.3 ff., also.

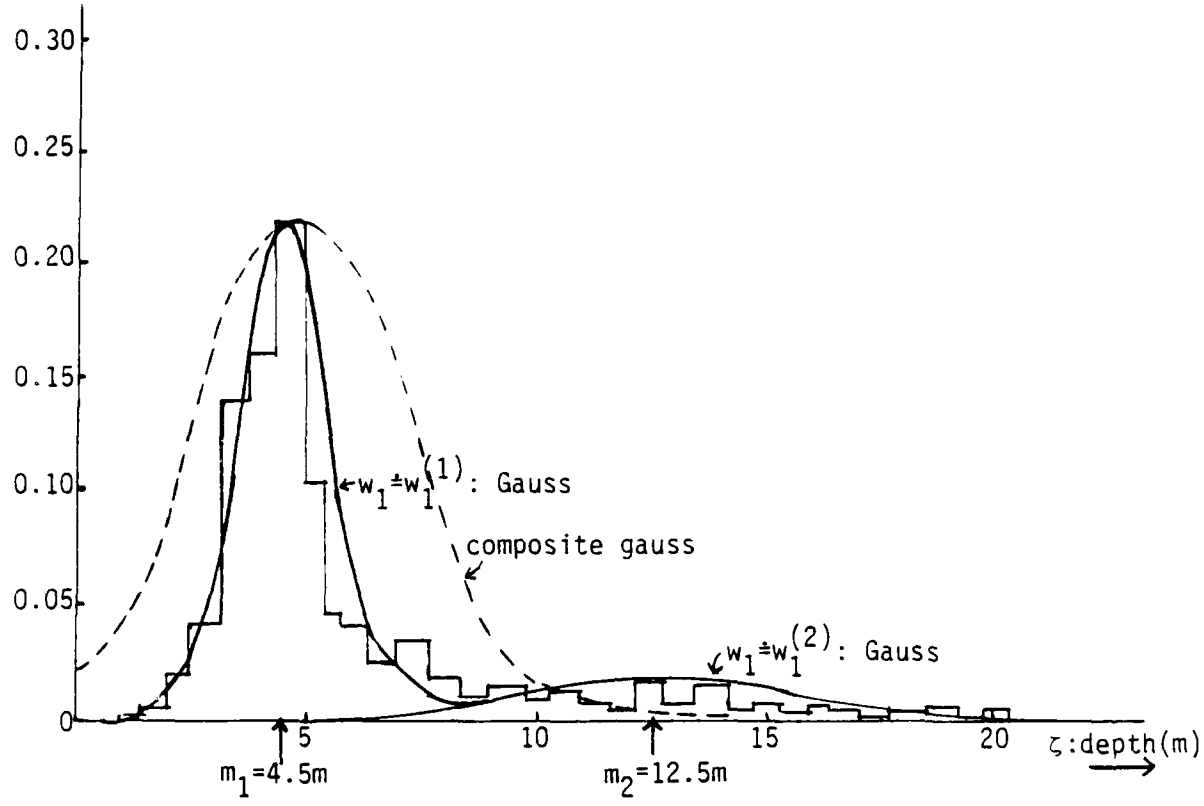

Figure 1.1: Histogram of underice profile ζ, from Lyon's data [1]; Ref. 4 of [2]. (Solid) curves: two component gaussian fit; dotted line: composite gauss, $\zeta = b_1\zeta_S + b_2\zeta_K$, cf. (2.7) et seq.

of widely separated nonzero mean profiles (elevations), e.g., m_S = 4.5 m vs m_K = 12.5 m, Fig. 1.1 (measured from the mean ocean surface), with appropriately small variances (σ_S, σ_K), cf. Fig. 1.1, ensures the practical vanishing of the pdf's w_{1S}, w_{1K}, etc., in question at $\zeta = 0$, as required (from the definition of the profile, cf. Fig. 2.1).*

---

*This latter requirement, viz. $\zeta \geq 0$, has suggested that Rayleigh processes for ζ_S, ζ_K may provide appropriate models, but direct attempts to construct Model I using such processes, as well as linear combinations of ζ_S and ζ_K (Model II), also indicate rather poor fits to the data, as does the process, $\zeta^2 = \zeta_S^2 + \zeta_K^2$, [7] (not shown on Fig. 1.1).

While the tangent plane approach of [4], as used here, for example, is applicable for f_o = O(≥ 50 Hz), it is not suited to situations where $k_o \ell_c$ is not large, cf. (3.1)-(3.3). We must then use the Method of Small Perturbations (MSP) for lower frequencies O(≤ 30 Hz) where the Rayleigh parameter is small; see Secs. 9.1-9.6 of [11], esp. Sec. 9.6 vs. Sec. 3 of [5]; for MSP generally, see [12], Chapter 3. At these low frequencies, the coherent-scattered energy, in the specular direction, dominates the incoherent scattered energy. This is the reverse of the "high-frequency" or large Rayleigh number cases, where now the surface has a large (vertical) roughness scale, so that coherence is destroyed, even in the specular direction, and only the incoherent scatter is observable, cf. (2.15)-[4] vs. (2.13)-[4]. In our present study, as noted earlier, we shall consider only the intermediate and "high" frequency situations, when $k_o \ell_c$ >(>) 1 is obeyed.

3.1 Scattering Cross Sections: Model Ia

Model Ia, cf. Fig. 2.2b and Sec. 2.1, consists of a single surface,

$$\boxed{\underline{\zeta} = \hat{\underline{i}}_z \zeta_\Lambda = \hat{\underline{i}}_z (\zeta_L + \zeta_H),} \tag{3.5}$$

which we arbitrarily divide into low- and high-wave number portions, analogous to the treatment of ocean wave surfaces (Sec. 2.1, p. 6, and Eq. 2.1 of [4]). The reason for this, of course, is that the low-wave number part provides the "facet" or "optical" scatter components while the high-wave number portion is associated with the Bragg scatter terms--all under the condition here, (3.3), for the Kirchoff or tangent plane method [$f_o \geq$ O(50 Hz)], cf. [13].

The scattering cross sections $\hat{\sigma}_{inc}^{(0)}$ for the incoherent component of reradiation are defined and discussed in Appendix A.2.1 (see also Sec. 2.2 of [4]). For Model Ia, (3.5), we have here the first two terms of (2.13)-[4] for the "high-frequency" régimes, i.e., large Rayleigh numbers, e.g., $f_o \geq$ O(1 kHz), cf. Table 3.1:

Our general conclusion from the above is that for the ice profile of the Lyon data types [1], [5], cf. (2.9), we may consider the tangent plane or Kirchoff method of scattering analysis to be applicable (with appropriate corrections O(1-3 db), as usual, for small grazing angles, cf. remarks pp. 3, 37, 44), for frequencies above O(50 Hz), and possibly above 30 Hz. [For convenience, we shall designate the "intermediate frequency range" as O(0.10 kHz - 1 kHz) here, with the "high-frequency region" defined as O($\geq$ 1 kHz).]

The Rayleigh numbers, R_ζ, for these surfaces and frequencies, are typically (for $\sigma_\zeta^2 = 5.68 = (2.38)^2$ (m^2), cf. (2.6)) and small grazing angles, here $\theta_{oT} = 80°$ (for which $\cos\theta_{oT} = 0.174$):

$$R_\zeta = \sigma_\zeta^2 b_o^2 k_o^2 = (k_o \sigma_\zeta 2 \cos\theta_{oT})^2, \quad \text{(backscatter)}, \quad \text{cf. Eq. (A.2-12)}, \quad (3.4a)$$

$$= (0.828\ k_o)^2 \quad , \quad \theta_{oT} = 80° \quad , \quad (3.4b)$$

which for a range of intermediate frequencies, O(30 Hz - 1 kHz), is shown in Table 3.1 below. Frequencies O(30-50 Hz) are borderline for the applicability of the Kirchoff method, at any θ_{oT} (< 90°). We note that for small grazing angles ($\theta_{oT} \geq 80°$), f_o = (30-100+ Hz) are "low-frequency" from the viewpoint of the Kirchoff approach, i.e., have small Rayleigh numbers, while f_o = O($\geq$ 1 kHz) are "high-frequency," with large Rayleigh numbers. At larger grazing angles ($\theta_{oT} < 80°$) frequencies O($\geq$ 50 Hz) are all "high-frequency" in this sense.

Table 3.1 Rayleigh Numbers for Backscattering; $\theta_{oT} = 80°$

f_o (Hz): (sec^{-1})	λ_o (m)	$k_o = 2\pi/\lambda_o$ (m^{-1})	$R_{\zeta\text{-back}}$, Eq. (3.4b)
30	50	0.126	$1.09 \cdot 10^{-2}$
50	30	0.209	$3.00 \cdot 10^{-2}$
100	15	0.419	$1.20 \cdot 10^{-1}$
200	7.5	0.838	$4.82 \cdot 10^{-1}$
400	3.75	1.68	1.93
1 kHz	1.5	4.19	12.0
2 kHz	0.75	8.38	48.1

(i). The Kirchoff approach requires that $k_o \rho_c > (\gg) 1$; or $2\pi\rho_c/\lambda_o > (>) 1$, i.e., the local radius of surface curvature must be large compared to the incident wavelength, λ_o. This is equivalent to the condition

$$k_o \ell_c > (>) 1 \; ; \quad \ell_c = \text{(horizontal) correlation distance.} \tag{3.1}$$

(ii). For the (isotropic) bottom ice profile, (2.10b) gives the normalized directional correlation function $\rho_\zeta(\underline{\Delta r})$. From tables of $K_1(x)$, p. 737, [10], it is easily found that $xK_1(x) = e^{-1}$ at $x = x_{-1} = 1.65 = k_c \Delta r_{-1}$, so that, for $\Delta r_{-1} \equiv \ell_c$ we have

$$1.65(k_o/k_c) > (>) 1, \quad \text{or} \quad (\lambda_c/\lambda_o)(1.65) > (>) 1 \tag{3.2}$$

as a defining condition that the Kirchoff method is valid. Since, empirically, $k_c = 0.05$, we require

$$\frac{2\pi(1.65)}{0.05} > (>) \lambda_o, \text{ or } 2.07 \cdot 10^2 > (>) \lambda_o. \tag{3.3}$$

(iii). For $f_o = 30$ Hz, $\therefore \lambda_o = 50$ m, and $\therefore 2.07 \cdot 10^2 > (>) 50$, which is not a very strong inequality. However, for $f_o = 50$ Hz, $\lambda_o = 30$ m and $2.07 \cdot 10^2 > (>) 30$, which is better. At $f_o = 100$ Hz, $\lambda_o = 15$ m, and the inequality is ~14:1, which is sufficient. Moreover, defining ℓ_c according to the e^{-1}-scale, cf. (3.2), is quite strict: after $\rho_\zeta(\ell_c) = e^{-1} = 0.368$ there is still noticeable (radial) correlation left. We may therefore choose a distance such that $\rho_\zeta(\ell_{0.01}) = 0.01$, i.e., essentially negligible surface correlation, for which $k_c \ell_{0.01} \doteq 6.5$ (on using [10]), so that (3.3) is modified to $2\pi(6.5)/0.05 = 8.16 \cdot 10^2 > (>) \lambda_o$, which in turn permits a lower frequency, say 20 Hz (or $\lambda_o = 75$ m), for $8.16 \cdot 10^2/75 \doteq 11 > (>) 1$.

where again (2.14a,b) apply. Now, however, $\hat{\underline{n}}_K$ does not enter explicitly, cf. (2.15). The gaussian processes ζ_S, ζ_K, described statistically by (2.16a,b), still apply, as do the conditions (2.17). The statistics of δ_K noted in (2.18) must once more be evaluated, in any case.

2.4 A Model for the Marginal Ice Zone (MIZ) (Model IIb)

Model IIb above is also a reasonable candidate to describe the combined presence of ice and open water which is typical of the Marginal Ice Zone (MIZ). Now we replace the keels (in Λ_K above (2.19)) by the (plate) ice, e.g., $\zeta_K \to \zeta_I$, $\underline{r} \in \Lambda_I$, and $\zeta_S \to \zeta_{\text{ocean surface,S}}$, $\underline{r} \in \Lambda - \Lambda_I \notin \Lambda_I$, e.g.,

$$\left.\begin{aligned} \zeta(\underline{r},t) &= -\hat{\underline{i}}_z \zeta_I(\underline{r},t), \quad \underline{r} \in \Lambda_I; \\ &= -\hat{\underline{i}}_z \zeta_S(\underline{r},t), \quad \underline{r} \in \Lambda - \Lambda_I \notin \Lambda_I \end{aligned}\right\}, \tag{2.20}$$

where $\zeta_I = \zeta_I(\underline{r})$ if there is no relative motion of the ice vis-à-vis the platform in question (cf. (2.8) et seq.). Now $\zeta_S(\underline{r},t)$ represents the (moving) ocean wave surface, as before, which is subject to wave generation by the wind, in the usual way [vide Sec. 1, Sec. 2.1, of [4]].

The further development of the analysis for Models IIa,b, including the desired scattering cross sections, is reserved to a subsequent report. We continue here with Model I only.

3. Scattering Cross Sections for Model Ia

Here we make direct use of the results and derivations of the author's recent study [4]. We shall accordingly refer to specific relations therein by equation number, with -[ ] suffixed, e.g., (2.13) of [4] becomes (2.13)-[4], etc.

Since our analysis is based on the Kirchoff or tangent plane approach, the results are mainly applicable in the intermediate through "high frequency" ranges, which may be numerically established here from the following argument:

posed processes, then $W_1(k)$ is a sum of two separate processes, so that ρ_S and ρ_K may overlap (in wave-number) space. This partition is then made on the basis of the relative contributions to the total process, i.e., on an intensity basis, as indicated empirically by the parameters σ_S, σ_K in (2.2) and (2.16a,b):

(2). ζ_K, ζ_S are independent, by the argument of Sec. 1 above;

(3). δ_K is independent of ζ_S, ζ_K (and $\therefore$ $(\delta_{x,y})_K$: the location of the keel is independent of keel elevation, as well as of the smaller-scale surface component, ζ_S.

(4). δ_K can be: (i), quasi-periodically distributed [in the (x',y')-plane]; or
(ii), entirely randomly distributed in this plane, so that overlapping keels are possible. (2.17)

In the analysis leading to scattering cross-sections (and spectra where appropriate, i.e., moving platforms), we shall need the following statistics for δ_K:

$$<\delta_K> \; ; \; <\delta_{K1}\delta_{K2}> = <\delta_K(\underset{\sim}{r}_1,t_1)\delta_K(\underset{\sim}{r}_2,t_2)> = \hat{m}_\delta(\underset{\sim}{\Delta r},\tau), \tag{2.18}$$

again with the usual assumptions of homogeneity and isotropy, cf. (2.7) et seq. From (2.14b) it follows that $\hat{m}_{\delta|max} = 1 = \hat{m}_\delta(0,0)$, at least, while $\lim_{|\underset{\sim}{\Delta r}|\to\infty} \hat{m}_\delta \leq 1$, cf. (2.17); $1 > <\delta_K> > 0$, also from the fact that $\Lambda_K > 0$. These averages will be obtained explicitly by a direct extension of the author's results, Secs. 4.3, 4.5 of [6], to two dimensions (in a subsequent study, cf. Sec. 4 ff.).

where Λ_K is the region occupied by the keels, cf. Fig. (2.2a). [The positive z-direction is upward from the reference (x,y)- and parallel (x',y')-planes, with $\underset{\sim}{r} = \hat{\underset{\sim}{i}}_x x + \hat{\underset{\sim}{i}}_y y = \hat{\underset{\sim}{i}}_x x' + \hat{\underset{\sim}{i}}_y y'$, etc.] In terms of the subsequently required integrals over the domains of acoustic "illumination" of the underice surface we have

$$\underset{\sim}{r} \in \Lambda_K \rightarrow \int_\Lambda \delta_K(\underset{\sim}{r},t)(\ )d\Lambda \ ; \ \underset{\sim}{r} \in (\Lambda-\Lambda_K) \rightarrow \int_\Lambda [1 - \delta_K(\underset{\sim}{r},t)](\ )d\Lambda, \qquad (2.14a)$$

with

$$\delta_K = 1, \quad r \in \Lambda_K \ ; \qquad = 0, \ \underset{\sim}{r} \in \Lambda_K. \qquad (2.14b)$$

Here $\hat{\underset{\sim}{n}}_K$ is the unit normal to the ice-keel surface component, given by

$$\hat{\underset{\sim}{n}}_K = \left\{(\hat{\underset{\sim}{i}}_x \zeta_x + \hat{\underset{\sim}{i}}_y \zeta_y - \hat{\underset{\sim}{i}}_z)/\sqrt{1 + \zeta_x^2 + \zeta_y^2}\right\}_K \ ; \qquad (2.15)$$

$$= -\hat{\underset{\sim}{i}}_z \text{ when } \underset{\sim}{r} \in \Lambda_K: \ \zeta_x = \frac{\partial \zeta}{\partial x} \text{ , etc.}$$

The following assumptions and conditions are next imposed:

(1). ζ_K, ζ_S, and $\therefore$ ζ_{Kx}, ζ_{Ky}, are gauss processes, now with the c.f.'s

$$F_1(i\xi)_S = e^{-im_S\xi - \sigma_S^2\xi^2/2} \ ; \ F_2(i\xi_1,i\xi_2)_S = e^{-i\xi_1 m_S - i\xi_2 m_S - (\sigma_S^2/2)[\xi_1^2+\xi_2^2+2\xi_1\xi_2\rho_S]} \qquad (2.16a)$$

$$F_1(i\xi)_K = e^{-im_K\xi - \sigma_K^2\xi^2/2}; \ F_2(i\xi_1,i\xi_2)_K = e^{-i\xi_1 m_K - i\xi_2 m_K - (\sigma_K^2/2)[\xi_1^2+\xi_2^2+2\xi_1\xi_2\rho_K]}, \qquad (2.16b)$$

where m_S, σ_S, m_K, σ_K are given (in the case of Lyon's data) by (2.3), and we have taken account of the fact that the underice elevations are negative in our reference system, cf. Fig. (2.2a). Here ρ_S and ρ_K are normalized directional covariances of these elevations. From the isotropic assumptions of the empirical fit to the Lyon's profile given by Mellen et al. [5], ρ_S and ρ_K are to be obtained by some suitable partition of $W_1(k)$, (2.9), or $W_2(k,\phi)$, (2.11b). If we follow the underlying assumption of Model IIa above here that the S- and K-surfaces are super-

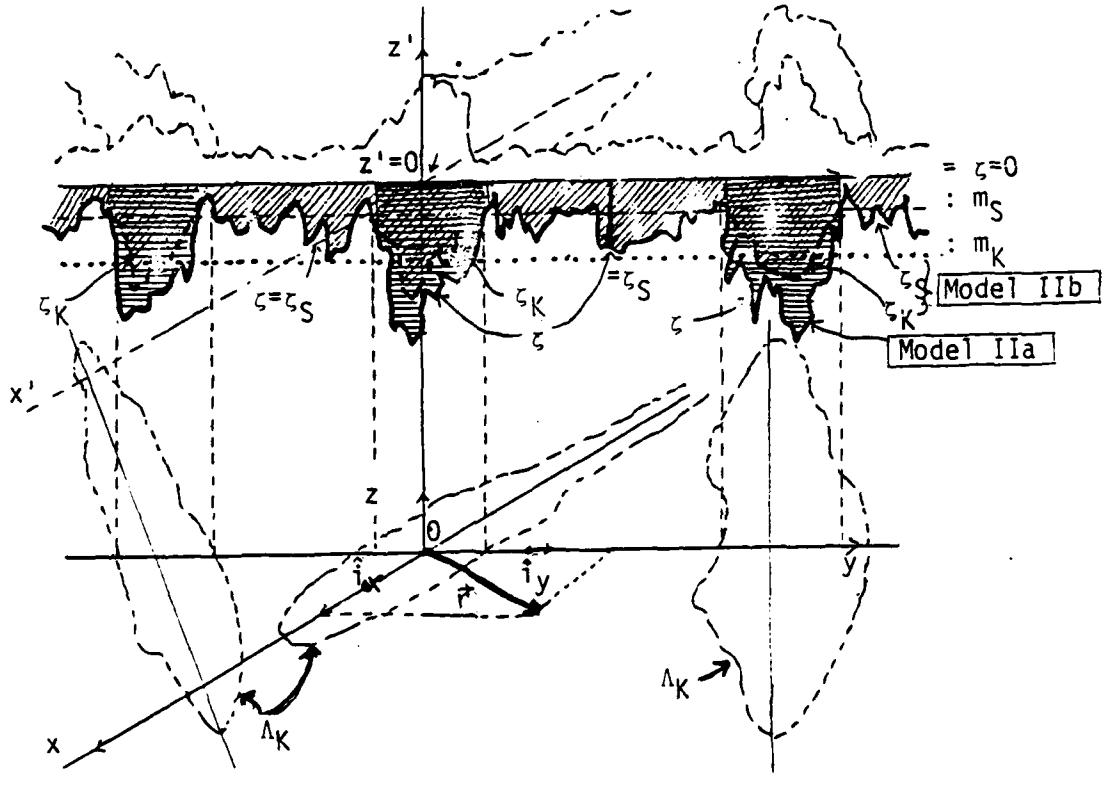

Figure 2.2a: Model II: Two-dimensional underice profiles (ζ), Eq. (2.13), with distinct keels (ζ_K); Λ_K are the (random) regions, projected onto the (x,y)- or (x',y':ζ=0) planes, by the specific keel structure. Model IIa: ζ_S rides on ζ_K; Model IIb: ζ_S and ζ_K are spatially separate.

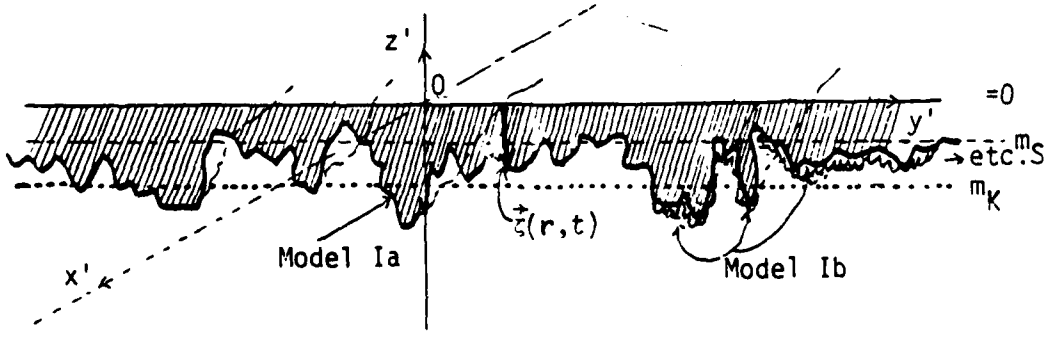

Figure 2.2b: Model I: Cross section of a (two-dimensional) underice profile (ζ), without distinct keels, governed by Eqs. (2.1)-(2.7). Model Ia has no separate roughness component; Model Ib has an (independent) roughness component riding on the large-scale profile.

(gaussian) underice profiles, ζ, of Model I, where keel structure, as such, is implicitly subsumed in the profile statistics, cf. Fig. 1.1. Two variants of Model I will be examined: Model Ia, which is a single-surface model, is the simplest choice, and one which we shall find needs to be extended, to account for observed scattering cross sections. This extension is Model Ib, which now includes an additional small-scale roughness component, riding on the single-surface.

Before we continue on to the results for scattering cross sections in Sec. 3 ff. for Model I, let us concisely describe Model II, which is a viable alternative to Model I, at least in those interactions where a keel structure can be identified. As in the case of Model I, two variants of Model II appear plausible: Model IIa, which is characterized by a comparatively small-scale (small $\bar{m}$, σ) elevation process which rides upon the (quasi-) random keel structure (large $\bar{m}$); and Model IIb, where the "small-scale" profile and the keel profiles occur separately in space. This latter form also appears reasonable for modeling the Marginal Ice Zone (MIZ) cases.

2.2 Model IIa: A Two-Component (Two-Dimensional) Underice Profile, with Keels

For this model we postulate that there is a distinct keel structure, with profile component ζ_K, upon which "rides" the smaller-scale bottom irregularities, whose profile component is ζ_S, in the manner of Fig. 2.2a. This is to be contrasted with our unstructured two-component model (Sec. 2.1), where no explicit keel structure is distinguished but is regarded as part of a single profile, ζ, governed by (2.1) etc., as sketched in Fig. 2.2b.

Accordingly, the underice profile for our Model II can be expressed as*

$$\left.\begin{aligned} \underline{\zeta}(\underline{r},t) &= -\hat{\underline{i}}_z\zeta_K(\underline{r},t) + \hat{\underline{n}}_K(\underline{r},t)\zeta_S(\underline{r},t), \qquad \underline{r} \in \Lambda_K \quad ; \\ &= -\hat{\underline{i}}_z\zeta_S(\underline{r},t) \qquad\qquad\qquad\qquad \underline{r} \in (\Lambda - \Lambda_K) \notin \Lambda_K \quad , \end{aligned}\right\} \tag{2.13}$$

---

*The time-dependence is indicated explicitly, to include possible platform motion, cf. (2.8) et seq.

from Appendix I, where $K_1(x)$ is a modificed Bessel function of the second kind. The corresponding transform relation is

$$W_1(k)_\zeta = \sigma_\zeta^2 \int_{-\infty}^{\infty} e^{ik\Delta r}\, \rho_\zeta(\Delta r)d(\Delta r) = \text{Eq. (2.9), etc.} \tag{2.10c}$$

The associated two-dimensional wave number intensity spectrum for this isotropic model is accordingly given by

$$W_2(k,\phi)_\zeta = \sigma_\zeta^2 \int_0^{\infty} \rho_\zeta(\Delta r)J_0(k\Delta r)\Delta r d(\Delta r) \tag{2.11a}$$

$$= 4\pi C/(k_c^2+k^2)^2, \quad 0 \leqslant \phi \leqslant 2\pi, \quad k = \sqrt{k_x^2+k_y^2}, \tag{2.11b}$$

in which

$$\sigma_\zeta^2 = \int_0^{2\pi} d\phi \int_0^{\infty} W_2(k,\phi)kdk = 2\int_0^{\infty} W_1(k)dk = C_1/k_c^2 < \infty, \tag{2.11c}$$

cf. Eq. (4) of [5], and Appendix I. We note that while σ_ζ^2 can be anatomized into the component contributions of ζ_S, ζ_K, cf. (2.5), (2.6), it is not possible to do this for the covariance or wave number spectrum (2.8)-(2.11) in our present Model I.

For these empirical models (2.9), (2.11) clearly σ_ζ^2 is finite, as it should be. However, we note that the corresponding wave number spectra of the profile slopes, ζ_x, ζ_y, or $\partial\zeta/\partial x$, etc., are

$$W_1(k)_{\partial\zeta/\partial x} = k^2 W_1(k)_\zeta \; ; \quad W_2(k,\phi)_{\zeta_{x=y}} = k^2 W_2(k,\phi), \tag{2.12}$$

so that the mean-square slopes $\sigma_{\zeta x,y}^2$ are logarithmically divergent. Of course, physically this is not acceptable, and we must therefore require a faster fall-off of the model $W_{1,2\zeta}$ with wave number, at the high frequencies. As yet there do not appear available data which allow us to extend the results of Fig. (2.1) beyond $\lambda_0 < 6$ m. Consequently, we are unable at this time to determine $\sigma_{\zeta x,y}$; (see, however, Sec. 3 ff.).

On the whole, nevertheless, with (2.5), (2.6), (2.9), (2.10) in (2.4) for $F_1(i\xi)_\zeta$ and (2.7) for $F_{2\zeta}$ we are specifically equipped to use the author's recently developed methods and results [4], (1984) formally to obtain the desired scattering cross-sections for the composite

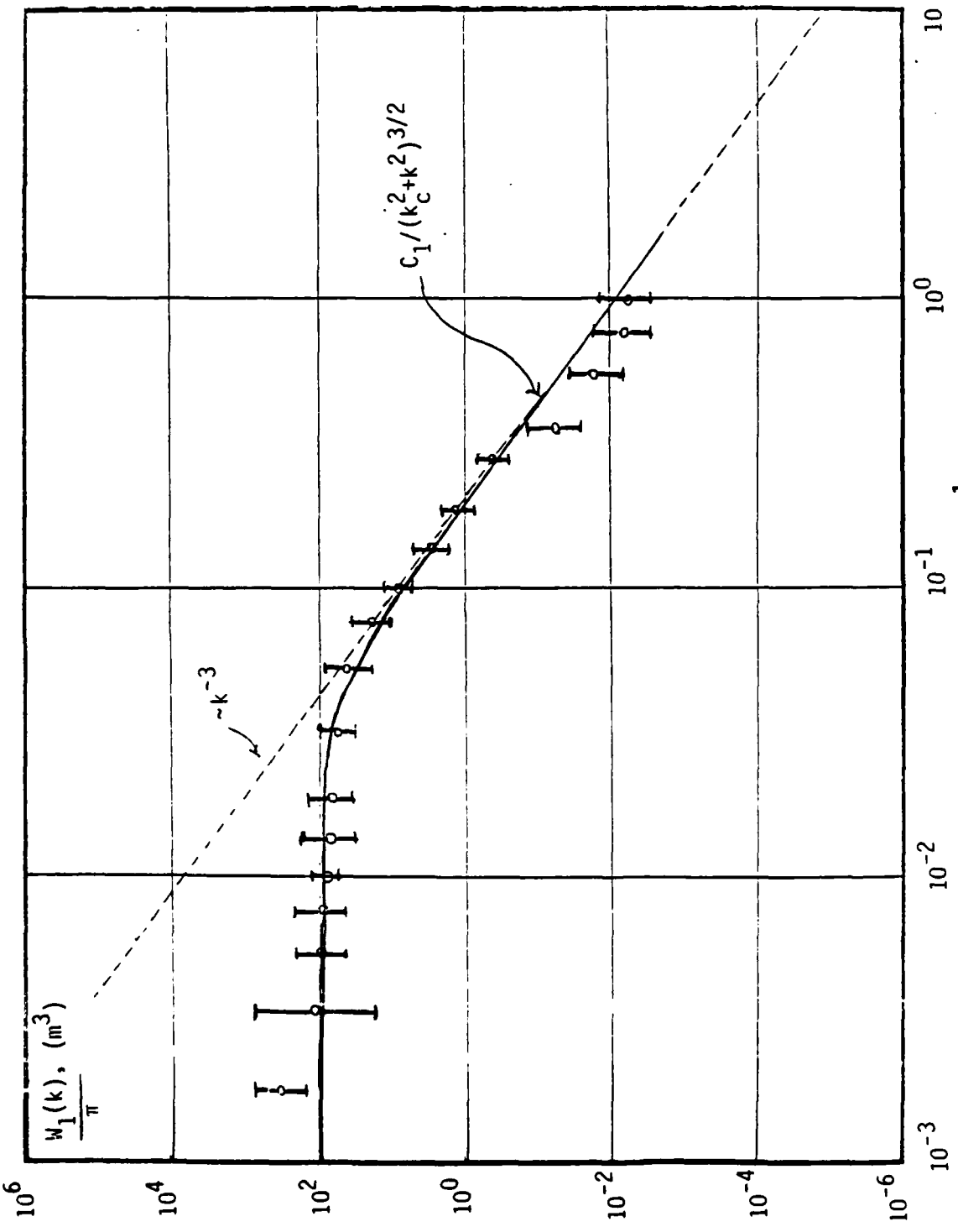

Figure 2.1: Roughness wave number (intensity) spectrum of underice profile ζ (circles), after Mellen et al. [5], from FFT of Lyon's data [1], Fig. 1.1. Solid line = empirical fit by Eq. (2.9) to the spectral data; "dc" component removed.

The new quantity ρ_ζ is the normalized covariance of the (possibly) relatively moving) underice surface elevation, defined by

$$\left.\begin{aligned}\rho_\zeta(\underset{\sim}{\Delta r},\tau=|\underset{\sim}{\Delta r}|/v_p) &= \{\overline{\zeta(\underset{\sim}{r}_1,t_1)\zeta_2(\underset{\sim}{r}_2,t_2)} - \overline{\zeta(\underset{\sim}{r}_1,t_1)}\cdot\overline{\zeta(\underset{\sim}{r}_2,t_2)}\}/\sigma_\zeta^2 \\ &= \{\overline{\zeta(\underset{\sim}{r}_1,t_1)\zeta(r_1+\underset{\sim}{\Delta r},t_1+\tau)} - \overline{\zeta(\underset{\sim}{r},t)}^2\}/\sigma_\zeta^2; \\ \underset{\sim}{\Delta r} &= \underset{\sim}{r}_2-\underset{\sim}{r}_1;\ \tau = t_2-t_1\ ,\end{aligned}\right\} \quad (2.8)$$

where $\underset{\sim}{r} = \hat{\underset{\sim}{i}}_x x + \hat{\underset{\sim}{i}}_y y$ is a vector in the (x,y)-reference planes, cf. Fig. (2.2a) ff., and v_p is the (uniform) speed of the reference platform. Thus, if there is platform motion, the (random) ice profile appears to be moving, like a random wave surface.* (With no relative motion $\rho_\zeta(\underset{\sim}{\Delta r},\tau)\to\rho_\zeta(\underset{\sim}{\Delta r},0) = \rho_\zeta(\underset{\sim}{\Delta r})$, as expected.) Note, as required, when $|\underset{\sim}{\Delta r}|\to\infty$, $\rho_\zeta\to 0$: there is no "dc"-component of ζ in ρ_ζ, and accordingly $F_2|_{\rho\to 0}=F_1(i\xi_1)F_1(i\xi_2)$, where F_1 is not given anymore by (2.4); cf. (2.6) et seq.

Next, we use Mellen et al.'s [5] isotropic empirical fit to the one-dimensional wave number (intensity) spectrum of the profile, Eq. (2), [5], obtained by FFT analysis of the profile shown in Fig. 1.1 with "dc" (or mean) component removed. This spectrum is (See Appendix I ff.):

$$\boxed{W_1(k)_\zeta = \pi C_1/(k_c^2 + k^2)^{3/2};} \quad C_1 = \sigma_\zeta^2 k_c^2 = 0.013;\ k_c = 0.05\ m^{-1}\ (\text{or } \lambda_c = 126\ m), \quad (2.9)$$

which is given in Figure 2.1. The standard deviation σ_ζ, of ζ_1, found from the analysis of these data is $\hat{\sigma}_\zeta = 2.3$ m, cf. remarks after Eq. (2) of [5], a result which is in excellent agreement with that of our composite model above, (2.6), namely, $\sigma_\zeta = 2.3\underline{8} = 2.4-$ (m). The associated (normalized) covariance function for (2.9) is ($v_p = 0$):

$$\rho_\zeta(\underset{\sim}{\Delta r}) = \frac{1}{2\pi}\int_{-\infty}^{\infty} dk W_1(k)_\zeta e^{-ik|\underset{\sim}{\Delta r}|}/\sigma_\zeta^2;\quad |\underset{\sim}{\Delta r}| = |r_2-r_1| = \Delta r, \quad (2.10a)$$

$$= \frac{1}{\pi}\int_0^{\infty} W_1(k)\cos k\,\Delta r\, dk/\sigma_\zeta^2 = k_c K_1(k_c\Delta r)\Delta r, \quad (2.10b)$$

---

*For random platform movement, in the general "bi-static" case of separate moving source and receiver platforms, see the author's 1977 paper, [9].

From well-known results ([6], Eqs. (1.30), (1.31)) we have the associated characteristic function (c.f.)

$$\boxed{F_1(i\xi)_\zeta \equiv \int_{-\infty}^{\infty} w_1(\zeta) e^{i\zeta\xi} d\zeta = b_1 e^{im_S\xi - \sigma_S^2\xi^2/2} + b_2 e^{im_K\xi - \sigma_K^2\xi^2/2}}, \quad (2.4)$$

with the following first and second moments

$$\bar{\zeta} = b_1 m_S + b_2 m_K = 5.1 \text{ (m)}; \quad \overline{\zeta^2} = b_1(\sigma_S^2 + m_S^2) + b_2(\sigma_K^2 + m_K^2) = 31.3 \text{ (m}^2\text{)} \quad (2.5)$$

$$\left.\begin{aligned} \therefore \sigma_\zeta^2 &\equiv \overline{\zeta^2} - \bar{\zeta}^2 \equiv \text{var } \zeta \\ &= b_1\sigma_S^2 + b_2\sigma_K^2 + b_1 m_S^2 + b_2 m_K^2 - (b_1 m_S + b_2 m_K)^2 \\ &= b_1\sigma_S^2 + b_2\sigma_K^2 + b_1 b_2 (m_S - m_K)^2 \\ &= 5.68 \text{ (m}^2\text{)} = (2.38)^2 \text{ (m}^2\text{)} \end{aligned}\right\} \quad (2.6)$$

from (2.2). We note that if we assumed that the underice elevation ζ were a composite (gaussian) sum, e.g., $\zeta = b_1\zeta_S + b_2\zeta_K$, then $\bar{\zeta}$ is correctly given in (2.5), but then $\overline{\zeta^2} \neq \zeta^2_{comp}$, cf. (A.3-13). In fact, we show in Appendix A.3 that (I), it is not possible to construct a second-order gauss-composite process which reduces to (2.1) or (2.4).

On the other hand, we need primarily the second-order pdf (or c.f.) of the profile ζ, in order to determine the desired (incoherent) backscatter cross section. In view of (I), Appendix A.3, remarked on above, we must restructure our gauss-composite model to include one which has a (still gaussian) second-order pdf (and c.f.), again because of the Central Limit theorem argument cited in Sec. 1. Accordingly, we choose the composite gauss process $\zeta = b_1\zeta_S + b_2\zeta_K$, and require it to have the same first-order first and second moments as (2.1) above, cf. (2.5), (2.6), accepting the rather poor first-order fit to the data, cf. Fig. 2.1. [For the coherent scatter cross sections we would use the well-fitted results (2.1) and (2.4) directly.] Consequently, the following second-order characteristic function, from Eq. (7.10) of [6], can be written

$$\boxed{F_2(i\xi_1, i\xi_2|\rho_\zeta) = e^{i\xi_1\bar{\zeta} + i\xi_2\bar{\zeta} - \sigma_\zeta^2[\xi_1^2 + \xi_1^2 + 2\xi_1\xi_2\rho_\zeta]/2}; \; (\zeta = b_1\zeta_S + b_2\zeta_K),} \quad (2.7)$$

where we have postulated homogeneity (and stationarity) for our present model. Here $\bar{\zeta}$ and σ_ζ^2 are given by (2.5), (2.6).

2. Underice Surface Elevation Models: I and II

Here we lay the statistical foundation for both our Models I and II, referred to above in Sec. 1, although in this Report we shall use only Model I in carrying out our determination of the desired scattering cross sections. Accordingly, let us begin with Model I.

2.1 Model I: An Unstructured Two-Component Underice Profile

From our fit to the Lyon histogram illustrated in Figure 1.1 we obtain the following first-order pdf* for the underice "profile" or surface elevation :

$$w_1(\zeta) = \frac{b_1}{\sqrt{2\pi\sigma_S^2}}\, e^{-(\zeta-m_S)^2/2\sigma_S^2} + \frac{b_2}{\sqrt{2\pi\sigma_K^2}}\, e^{-(\zeta-m_K)^2/2\sigma_K^2}\,, \tag{2.1}$$

where we find that, specifically,

$$\left.\begin{aligned} &b_1 = \frac{a_1}{a_1+a_2} = 0.93; \quad b_2 = \frac{a_2}{a_1+a_2} = 0.070; \quad a_1 = 0.22; \quad a_2 = 0.016; \\ &\qquad\qquad\qquad\qquad\qquad\qquad\qquad\qquad \text{and } b_1+b_2 = 1.00; \\ &\left.\begin{aligned} m_S &= 4.50 \text{ m} \\ \sigma_S &= 1.00 \text{ m} \end{aligned}\right\} \;; \qquad \left.\begin{aligned} m_K &= 12.5 \text{ m} \\ \sigma_K &= 3.0 \text{ m} \end{aligned}\right\} . \end{aligned}\right\} \tag{2.2}$$

It is clear that

$$\int_0^\infty w_1(\zeta)d\zeta \doteq \int_{-\infty}^\infty w_1(\zeta)d\zeta = 1 \tag{2.3}$$

here, in view of the large means (m_S, m_K) and comparatively small variances, so that the "tails" of both the fitted gaussian densities are quite negligible for $\zeta < 0$. Thus, the underice "profile," or elevation ζ, is described by the weighted sum of two gaussian distribution (densities) (which is, of course, not the same as the composite gauss process consisting of the weighted sums of the separate elevations ζ_S, ζ_K, cf. Appendix A.3.) We call ζ here, cf. (2.1), a gauss-composite process.

---

*For the moment, in Model I, we regard ζ as positive downward; since z is positive upward, cf. Fig. (2.2a), in the platform-underice geometry of Section 3 ff., we will accordingly change the signs of $\bar{\zeta}$, etc. appropriately.

Because of the large Rayleigh numbers involved, theories based solely on Bragg scatter are inadequate, except at very low frequencies and/or large grazing angles. Consequently, we must develop the first- and second-order characteristic functions of the profile elevation ζ. Then, we must artificially decompose the single elevation process ζ (Model Ia) into two further (independent) processes at some sufficiently short surface wavelength, or corresponding wave number k_D ($=2\pi/\lambda_D$), so as to obtain the scattering contributions of the "rough" (i.e., Kirchoff "facets") and the "smooth" (or Bragg) surface components, just as is done in the conventional treatment of wind-wave surfaces as distinct gravity plus capillary wave surfaces [8]. (A similar approach is used for the large-scale surface component of Model Ib ff.)

The specific dichotomy depends, of course, on the wave number (intensity) spectrum of the underice surface (cf. Eq. 2.3 and Sec. 7.3C of [4]), examples of which are modeled in [2], [5] (Sec. 2) from empirical data. Thus, our theoretical approach in this work is a direct extension and modification of our earlier results [4], which provide the substantive analytical foundation of the present effort. We shall for the most part be content to present the needed final results, referring the reader to [4] for the detailed background. What is new here vis-à-vis earlier work [for example, [2], [5], and refs. therein] is (1), explicit statistical-physical models of the underice profile, which permit an incoherent as well as coherent scattering analysis at intermediate and high frequencies; and (2), the specific results of that analysis, albeit limited to Model I here. Model I itself is simplified basically to a single gaussian process, ζ, now with means and variances given by those of the first-order gauss-composite fit to the Lyon data [cf. (2.1), (2.2) et seq.]

Finally, this Report is organized as follows: Section 2 gives an analytic description of the aforementioned two profile models (I, II), with their pertinent statistics. Section 3 provides backscattering cross sections of Model Ia, and Section 4 includes the extension of Model Ia to Model Ib, to provide a possible mechanism whereby agreement between theory and experimental data can be effected. (A full treatment is reserved to a subsequent report.) Section 5 concludes our analysis with a concise summary of the principal results and conditions under which they apply. [Appendixes A.1-A.3 provide appropriate special results and analyses.]

$$\hat{\sigma}^{(0)}_{\text{inc } R_\zeta >> 1} = \overline{R_o^2}\ \overline{S_o^2} \left\{ \left(\frac{\alpha_{ox}^2+\alpha_{oy}^2+\alpha_{oz}^2}{\alpha_{oz}/2} \right)^2 \frac{e^{-\frac{1}{2b_o^2}\left[\frac{(2\alpha_{ox})^2}{\sigma_{Lx}^2}+\frac{(2\alpha_{oy})^2}{\sigma_{Ly}^2}\right]}}{8\pi b_o^2 \sigma_{Lx}\sigma_{Ly}} + \frac{k_o^4}{16\pi^2} N_{LH}^{(0)}\ (\underset{\sim}{2\alpha}_{o\perp})_{\text{inc}}\ W_H(\underset{\sim}{2\alpha}_{o\perp} k_o) \right\}_\zeta \tag{3.6}$$

The terms in { } represent the results of the "physical-optics" cum "perturbational" approach, i.e., here respectively the facet and Bragg scatter terms, cf. Sec. 7.3 of [4]. The former is seen to be independent of frequency, while the latter is a first-order Bragg component, since $\sigma_H^2 << 1$, or more precisely, $R_{H\zeta} << 1$, with small correlations.*

In (3.6), $N^{(0)}_{LH\text{-inc}}$ is a "tilt-factor," embodying the fact that the high-wave number surface component, ζ_H, is tilted, i.e., presents on the average a larger grazing angle $\phi(= \pi/2 - \theta_{oT})$ toward the plane of incident radiation. The quantity W_H is the wave numner intensity spectrum of ζ_H into which the (single) profile ζ, (3.5), is dichotomized, while σ_{Lx}^2, σ_{Ly}^2 are the variances of the (x,y)-slopes of the "low"-wave number component, ζ_L, of the underice surface in this model, cf. (3.5). (The symbol $\perp$ denotes (x,y)-plane or (x,y)-components only, and α_{ox}, etc., are differences of the components of the incident and reflected waves' unit vectors, $\hat{\underset{\sim}{i}}_T - \hat{\underset{\sim}{i}}_R$, for the basic one-reflection geometry of this study, viz. Figs. A.2-1, A.2-2; $b_o = \cos\theta_{oT} + \cos\theta_{oR}$. For a detailed description of the various elements of (3.6), and (3.7), (3.8) following, see Appendix A.2, including the reflection and shadowing factors ($\overline{R_o^2}$, $\overline{S^2}$) in Sec. 3.2 below.

For the coherent cases the scattering cross section is defined by (A.2-5) and is found for all Rayleigh numbers, $R_\zeta (> 0)$ such that the Kirchoff condition (3.1)-(3.3) is obeyed, here for $f_o (\geq O(50\text{ Hz}))$, to be

---

*This assumes a "splitting" wave number k_D large enough that

$$\sigma_H^2 = \int_{k_D}^{\infty} W_H(\underset{\sim}{k})\,\underset{\sim}{dk}/(2\pi)^2 << 1\ (m^2),\ \text{cf. Sec. 3.3}\underset{\sim}{C},\ \text{Eq. 3.21) ff.}$$

$$\hat{\sigma}_{coh}^{(0)} \simeq A_1 \frac{\overline{R_o^2}\,\overline{S^2}\,k_o^2}{16\pi^2} \left\{ (2\alpha_{oz})^2 \, e^{-b_o^2\sigma_\zeta^2 k_o^2} \cdot e^{-3k_o^2[\alpha_{ox}^2/A + \alpha_{oy}^2/B]} \right\} \quad \left. \right\} (3.7)$$

$$\to 0, \quad \text{"high-frequencies,"} \quad R_\zeta >> 1,$$

here for $f_o = O(\geq 1\ \text{kHz})$, cf. Table 3.1 above: very rough surfaces, e.g., $R_\zeta >> 1$, destroy coherence, as expected. [In addition, since the beam parameters $A,B << 1$, cf. (6.32)-[4], the second exponential also ensures the vanishing of $\hat{\sigma}_{coh}$, unless the Snell angle ($\alpha_{ox} = \alpha_{oy} = 0$) is chosen.] Note that this coherent-scatter cross section depends on the area illuminated (via A_1), as distinct from the incoherent cases, (3.6), which are always area-independent, subject, of course, to the conditions cited in (A.2-15). Our results (3.6), (3.7) hold for arbitrary directions of illumination and observation.

Various particular cases of (3.6), (3.7) can be obtained directly by appropriate specialization, e.g., "high"- and "low"-frequency back- and forward-(specular) scatter, etc., from the author's results, pp. 18-24 of [4] (always subject to the Kirchoff condition (3.3)-(3.4)). Since we shall show presently [Sec. 3.3] that Model Ia, (3.5), is apparently incapable of acceptable agreement with empirically measured cross sections, we shall limit our treatment to the special cases of <u>backscatter</u>, for which (3.6) reduces, on setting $\phi_{oT} = \pi/2$, cf. Fig. A.2-1, $\theta_{oR} = \theta_{oT}$, to

$$\hat{\sigma}_{inc}^{(0)}\Big|_{\substack{\text{back} \\ R_\zeta >> 1 \\ \theta_{oT}=\pi/2}} \simeq \overline{R_o^2}\,\overline{S^2} \left[\frac{e^{-\tan^2\theta_{oT}/2\sigma_{Ly}^2}}{8\pi\sigma_{Lx}\sigma_{Ly}\cos^4\theta_{oT}} + \frac{k_o^4}{16\pi^2} N_{LH}^{(0)}(\theta_{oT})_{inc} W_H(0, 2k_o \sin\theta_{oT}) \right] \quad (3.8)$$

$$\simeq \hat{\sigma}_{inc\text{-}L}^{(0)} + \hat{\sigma}_{inc\text{-}H}^{(0)} \Big\}_{R_\zeta >> 1}. \quad (3.8a)$$

Again, the first term of (3.8) is independent of frequency, in this "high-frequency" ($R_\zeta >> 1$) approximation, which as noted above is the "specular-point," facet, or geometrical acoustics solutional form of the "full-wave" approach of Bahar and Barrick et al. [13], [14], [15], (and also references [5], [22], [24], [31], [44] in [4]). The second

term of (3.8) embodies the (first-order) Bragg scatter associated with the small-scale surface component ζ_H. Whereas the specular-point contribution, $\hat{\sigma}^{(0)}_{inc\text{-}L}$, is the dominant part of the cross section for moderate to small θ_{oT}, it vanishes rapidly for small grazing angles (θ_{oT} large), so that in this surface model only the perturbational Bragg term, $\hat{\sigma}^{(0)}_{inc\text{-}H}$, contributes. We shall use this observation in Section 3.3 below to test the applicability of our Model Ia, (3.5).

3.2 The Reflection, Tilt-, and Shadowing Factors: $\overline{R_o^2}$, $N^{(0)}_{LH\text{-}inc}$, $\overline{S^2}$:

With wind-wave surfaces, which are pressure release surfaces, $(\rho c_o)_{water}/(\rho c_o)_{air} \sim \infty$. As a result the (local plane-wave) reflection coefficient R_o is $R_o \doteq -1$, cf. (3.9a) ff. Moreover, since the rms wave slopes are small $O(\leq 5 \cdot 10^{-2})$, the tilt-factor ($N^{(0)}_{inc}/16 = \hat{N}^{(0)}_{inc}$) is likewise small $O(10^{-2})$, cf. (3.2d,e)-[4], and unless $\theta_{oT} > 85°$, the shadowing coefficient $\overline{S^2}$ is always close to unity. With ice surfaces, however, these perturbational conditions do not fully hold: as we shall see from (3.9) below, at these frequencies $O(\geq 50$ Hz), R_o is +1, while quite large slopes $\sigma^2_{L(x=y)} = O(\leq 1.5)$ may occur. This, in turn, generates larger tilt-factors, as we would expect, and at the same time produces more shadowing. Consequently, we must reexamine our earlier evaluations of both the tilt-factors and shadowing coefficients used in our wave surface analyses [4], to take these modifications into account.

Accordingly, let us begin first with the reflection coefficient:

A. The (Plane-Wave) Reflection Coefficient, R_o

For our far-field application here the local plane-wave reflection coefficient R_o is a reasonable approximation, even when averaged and removed from under the integral sign in the Total Surface Spreading Function (TSSF), cf. (A.2.7a), as in (3.6)-(3.8). Specifically, we have

$$R_o(\theta_{oT}) = \frac{\rho_I c_I \cos\theta_{oT} - \rho_w c_w \cos\theta'_{oT}}{\rho_I c_I \cos\theta_{oT} + \rho_w c_w \cos\theta'_{oT}}, \qquad (3.9)$$

where $(\rho c)_I \doteq 2$ for ice and $(\rho c)_w = 1$ for water, and θ'_{oT} = angle of

transmission in the ice. Since at these frequencies (perfect) internal-reflection occurs for ice, $\theta'_{oT} = \pi/2$, and

$$R_o = \frac{2\cos\theta_{oT} - 0}{2\cos\theta_{oT} + 0} = 1. \tag{3.9a}$$

[For air-water interfaces $(\rho c)_{I\to air} << 1$, and so $R_o \doteq -1$, as usual.] Thus, R_o^2 is our scattering cross section here, and is given by

$$\boxed{\overline{R_o^2}\Big|_{ice} \doteq 1 = 0 \text{ db}.} \tag{3.10}$$

B. "Tilt-Factors" $N^{(0)}_{LH\text{-}inc}$, $\hat{N}^{(0)}_{LH\text{-}coh}$

From (8.28a)-[4], and from (7.22)-[4], (7.24)-[4], respectively, for the incoherent and coherent cases, we can write the "tilt factors" for Model Ia here as

$$N^{(0)}_{LH\text{-}inc} = (2\alpha_{oz})^2 \left\langle (2\alpha_{ox}\zeta_x + 2\alpha_{oy}\zeta_y - 2\alpha_{oz})^2 \right\rangle_L \quad , \zeta_x = \frac{\partial\zeta}{\partial x}, \text{ etc.} \tag{3.11}$$

For the symmetrically distributed slopes assumed here (about $\overline{\zeta_x} = \overline{\zeta_y} = 0$), (3.11) reduces directly to

$$N^{(0)}_{LH\text{-}inc} = (2\alpha_{oz})^2 \{(2\alpha_{ox})^2\sigma^2_{Lx} + (2\alpha_{oy})^2\sigma^2_{Ly} + (2\alpha_{oz})^2\},$$
$$\sigma^2_{Lx,y} \equiv \overline{\zeta^2_{x,y}} \quad , \tag{3.12a}$$

Choosing $\phi_{oT} = \pi/2$, cf. Figs. A.2-1,2, we get, cf. (A.2-11),

$$\boxed{N^{(0)}_{LH\text{-}inc}\Big|_{\phi_{oT}=\pi/2} = (2\alpha_{oz})^2 [(2\alpha_{oy})^2 \sigma^2_{Ly} + (2\alpha_{oz})^2].} \tag{3.12b}$$

Similarly, from (7.22)-[4], etc. we have

$$\hat{N}^{(0)}_{LH\text{-}coh} = \left\langle \frac{(2\alpha_{ox}\zeta_x + 2\alpha_{oy}\zeta_y - 2\alpha_{oz})^3}{1 + \zeta_x^2 + \zeta_y^2} \right\rangle_L = -8\alpha_{oz} \left\langle \frac{(6\zeta_x^2\alpha_{ox}^2 + 6\zeta_y^2\alpha_{oy}^2 + \alpha_{oz}^2)}{1 + \zeta_x^2 + \zeta_y^2} \right\rangle_L \tag{3.13}$$

taking advantage of the assumed symmetrical distribution of the slopes (where $\langle \zeta_x^3 \rangle = \langle \zeta_x \rangle = 0$, etc.).

Inasmuch as $\langle \phi_{x,y}^2 \rangle$ = mean-square slope angles of the profile, we have at once by definition

$$\boxed{\sigma_{Lx,y} = \tan \langle \phi_{x,y}^2 \rangle^{\frac{1}{2}}}, \quad \text{or} \quad \boxed{\langle \phi_{x,y}^2 \rangle^{\frac{1}{2}} = \tan^{-1} \sigma_{Lx,y}.} \tag{3.14}$$

Unlike surface waves, where $\sigma_{Lx=y}^2 = (5.42 \cdot 10^{-2})$ or $\langle \phi^2 \rangle^{\frac{1}{2}} = 13.1°$, cf. (3.2d)-[4], for 20 knot (mean) wind speeds, we may expect the slopes of the bottom ice profile to be considerably larger. This is borne out by (albeit limited) empirical data, which suggests that $\langle \phi^2 \rangle^{\frac{1}{2}} = O(30°)$, or $\sigma_{Lx,y}^2 = 3.33 \cdot 10^{-1}$, [16]. Consequently, we cannot replace $1 + \zeta_x^2 + \zeta_y^2$ by unity in (3.13), but must evaluate the averages exactly. We continue to assume isotropic bottom surfaces [cf. Sec. 2], e.g., $\sigma_{Lx} = \sigma_{Ly}$. Accordingly, since ζ is postulated to be gaussian, in accord with our Model I, cf. Sec. 2 above, so also are ζ_x, ζ_y, which are likewise independent of each other and of ζ. In fact, we can write explicitly

$$w_1(\zeta_{Lx}, \zeta_{Ly}) = \frac{e^{-\zeta_{Lx}^2/2\sigma_{Lx}^2 \; - \; \zeta_{Ly}^2/2\sigma_{Ly}^2}}{2\pi\sigma_{Lx}\sigma_{Ly}} = \frac{e^{-(\zeta_{Lx}^2+\zeta_{Ly}^2)/2\sigma_{L(x=y)}^2}}{2\pi\sigma_{L(x=y)}^2} \Bigg|_{\text{isotropic}} \tag{3.15}$$

with $\sigma_{Lx,y}^2 = \overline{\zeta_{Lx,y}^2}$. Using (3.15) in (3.13) allows us to write

$$\boxed{\hat{N}_{LH\text{-}coh}^{(0)} = -8\alpha_{oz} \{(6\alpha_{ox}^2 + 6\alpha_{oy}^2) I^{(2)}(a^2) + \alpha_{oz}^2\},} \tag{3.16}$$

where (cf. pp. 107, 108, [4])

$$I^{(2)}(a^2) \equiv \int_{-\infty}^{\infty} \int \frac{(x^2 \text{ or } y^2) e^{-(x^2+y^2)/2\sigma^2}}{1 + x^2 + y^2} \frac{dxdy}{2\pi\sigma^2} = \frac{a^2}{2} \int_0^{\infty} \frac{y e^{-a^2 y}}{1 + y} dy,$$

$$a^2 \equiv 1/2\sigma^2,$$

$$= \frac{1}{2} \{1 - a^2 \int_0^{\infty} \frac{e^{-a^2 y}}{1 + y} dy\} = \frac{1}{2} \{1 + a^2 e^{a^2} Ei(-a^2)\}, \tag{3.17}$$

since

$$\int_0^\infty \frac{e^{-a^2 z}}{1+z}\,dz = -e^{a^2}\,Ei(-a^2); \quad \text{with } -e^{a^2}\,Ei(-a^2) \simeq a^{-2}\sum_{m=0}^{\infty}(-1)^m\, m!\,a^{-2m},\ a^2>>1, \tag{3.17a}$$

and $-Ei(-x) = Ei(x)$ is tabulated in [17], [18]. Table 3.2 and Fig. 3-1 below show $N^{(0)}_{LH\text{-}inc}$ and $\hat{N}^{(0)}_{LH\text{-}coh}$ for a range of rms profile slopes.

C. Shadowing Factor, $\overline{S^2}$

We shall limit ourselves here to the incoherent backscatter cases (R@T) only, for this study. [A summary of pertinent results for $\overline{S^2}$ and $\overline{S}$ (R@T) is given in C, Sec. 7.4, [4], cf. p. 109.] Here $S^2_{back} = \tilde{Q}(\psi = \phi)$, Fig. 59 of [12], where $\phi(= \pi/2 - \theta_{oT})$ is the grazing angle, as before. The pertinent parameter here is

$$\left.\begin{aligned} \hat{a} &\equiv (\cot\theta_{oT})/\sigma_{L(x=y)} \quad (\equiv \alpha \text{ of Fig. 59, [12]}),\\ &= (\tan\phi)/\sigma_{L(x=y)} \end{aligned}\right\} \tag{3.18}$$

By calculating $\hat{a}$ ($\equiv \alpha$) and using Fig. 59, [12] we at once obtain good estimates of S^2_{back} ($= \hat{Q}$). For the large rms underice profile slopes encountered here we see that $\langle\zeta^2_{back}\rangle$ can be noticeably reduced from unity (no effective shadowing), vide Table 3.2 (and Fig. 3.1), again unlike the ocean wave surface environments commonly encountered, where $\sigma^2_{(x=y)}$ is comparatively small, C, Sec. 7.4 of [4], where $S^2_{back} \sim 1$.

Table 3.2 Backscatter, $\theta_{oT} = 80°$; ($\phi_{oT} = \pi/2$)

rms slope angles, $\langle\phi^2_L\rangle^{\frac{1}{2}}$	σ_L	σ^2_L	db	$N^{(0)}_{LH\text{-}inc}/16$	$\hat{N}^{(0)}_{LH\text{-}coh}/16$	db	$N^{(0)}_{LH\text{-}inc}/16$	$\hat{a}_{80°}$	$\overline{S^2_{back}} = \tilde{Q}$	(db)
0	0	0	(-30.4)	$9.09\cdot10^{-4}$	$4.20\cdot10^{-2}$	(-30.4)	$9.09\cdot10^{-4}$	∞	1.00	0.0
10	0.176	$3.11\cdot10^{-2}$	(-27.4)	$1.82\cdot10^{-3}$	(0.35)		$O(10^{-2})$	1.00	0.96	-0.2
20	0.364	$1.32\cdot10^{-1}$	(-23.2)	$4.77\cdot10^{-3}$	0.826	(-13.7)	$4.27\cdot10^{-2}$	$4.84\cdot10^{-1}$	0.80	-1.0
30	0.577	$3.33\cdot10^{-1}$	(-19.7)	$1.06\cdot10^{-2}$	1.37	(-8.2)	$1.50\cdot10^{-1}$	$3.06\cdot10^{-1}$	0.63	-2.0
40	0.839	$7.04\cdot10^{-1}$	(-16.7)	$2.15\cdot10^{-2}$	1.95	(-4.3)	$3.72\cdot10^{-1}$	$2.10\cdot10^{-1}$	0.49	-3.1
50	1.19	1.42	(-13.7)	$4.24\cdot10^{-2}$	2.35	(-0.7)	$8.52\cdot10^{-1}$	$1.48\cdot10^{-1}$	0.37	-4.3
	Eq. (3.14)		Eq. (3.19a)		Eq. (3.19b)		Eq. (4.7)	Eq. (3.18)	Fig. 59, [12]	

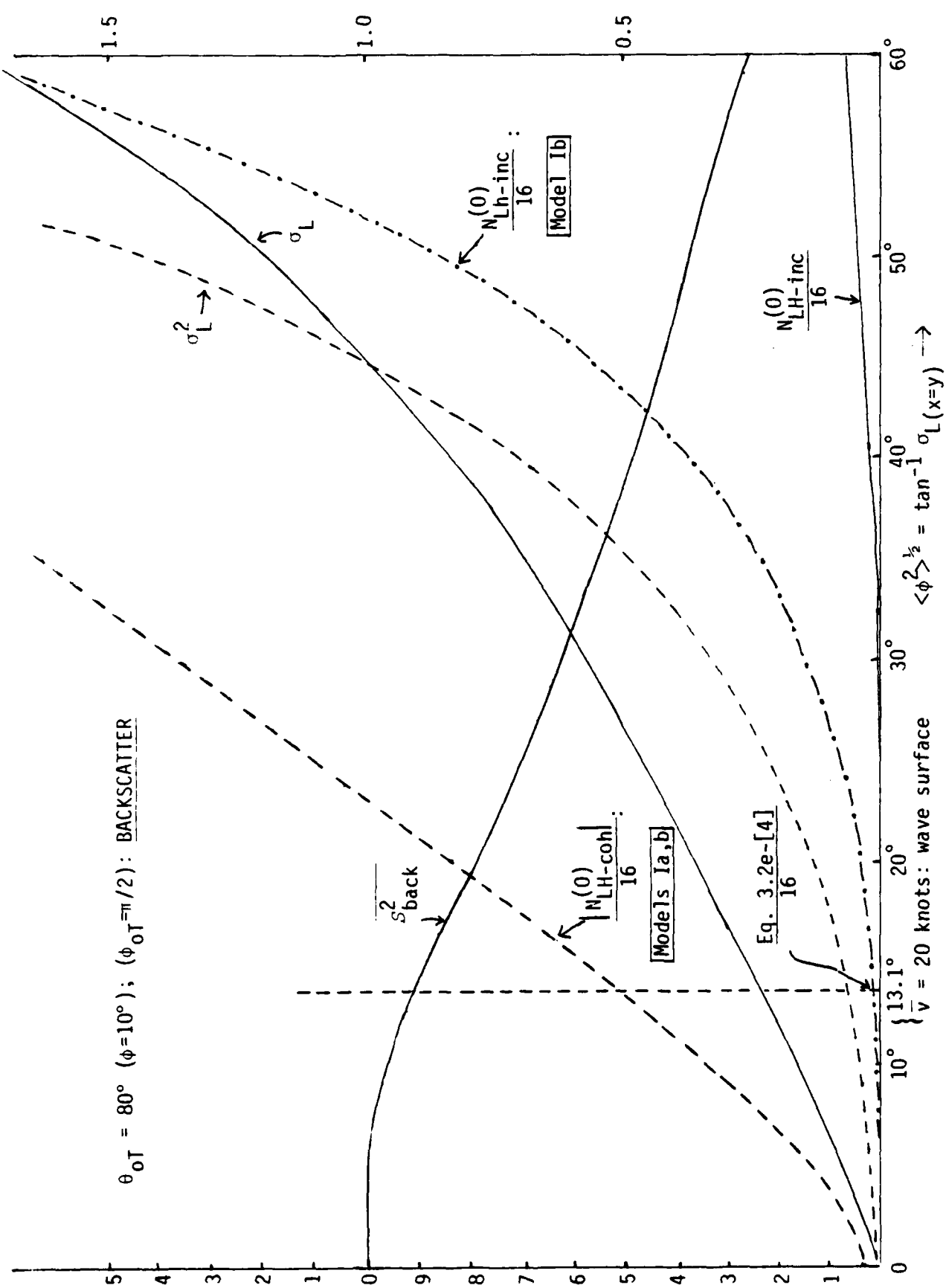

Figure 3.1 Parameters of the Ice-Bottom Scattering Models (Models Ia, Ib).

For the backscatter condition taken here ($\theta_{oT} = 80°$; $\phi_{oT} = \pi/2$), Eqs. (3.12b), (3.16) reduce, cf. (A.2-13), to

$$\theta_{oT}=80°;\quad (\therefore\ \phi=10°)\quad \begin{cases} \left.\dfrac{N^{(0)}_{LH\text{-}inc}}{16}\right|_{\substack{back\\ \phi_{oT}=\pi/2}} = \cos^4\theta_{oT}\{\sigma_L^2\tan^2\theta_{oT}+1\} \\ \qquad = 9.09\cdot 10^{-4}\{(32.16)\sigma_L^2+1\}, \end{cases} \tag{3.19a}$$

$$\begin{cases} \left.\dfrac{\hat{N}^{(0)}_{LH\text{-}coh}}{16}\right|_{\substack{back\\ \phi_{oT}=\pi/2}} = -8\cos\theta_{oT}\{6I^{(2)}(a^2)\sin^2\theta_{oT}+\cos^2\theta_{oT}\} \\ \qquad = -1.39\{5.82I^{(2)}+3.02\cdot 10^{-2}\}. \end{cases} \tag{3.19b}$$

Figure 3.1 shows how σ_L, σ_L^2, $N^{(0)}_{LH\text{-}inc}$, etc. vary with the rms slope angle. Typical values of $\langle\phi^2\rangle^{1/2}$ are $O(30°)$ for ice bottom profiles, [16]. As expected, increasing $\langle\phi^2\rangle^{1/2}$ leads to increasing tilt-factors and smaller shadowing coefficients ($\overline{S^2}$), because on the average, the effective angle of incidence is thus increased over θ_{oT} as a result of the larger (bottom) slopes. Also, for the same reason, the fraction of the scattering surface cast in shadow is increased, i.e., $\overline{S^2}$ is decreased. However, comparison of $\overline{S^2}$ (db) and $N^{(0)}_{LH\text{-}inc}$ (db) from Table 3.2 shows that the tilt-factor increases (with σ_L or $\phi^{2\,1/2}$) considerably more rapidly than the shadowing factor decreases, so that the net effect is a significant (relative) gain in scattering strength due to the increasing rms slopes of the bottom ice surface, as this may occur. Note, for the ocean wave example discussed in Sec. 3.1 of [4], that the rms slope angle is 13.1° (corresponding to a mean wind speed $\bar{v} = 20$ knots), cf. Eq. 3.2e-[4], for which $\sigma_L = 0.233$, from (3.14), with $\overline{S^2}_{back} = -0.4$ db, as shown on Fig. 3.1 here. In this case the associated tilt-factors are comparatively small.

3.3 Model Ia: A Numerical Example--Incoherent Backscatter at $\theta_{oT} = 80°$, $f_o = 1$ kHz

With the results of Sec. 3.2 in hand, let us apply them to Eq. (3.8) to obtain the (theoretical) backscatter cross section for a critical geometry, which tests the adequacy of our physical model. Such a test

occurs at "high frequencies" and small grazing angles, where the geometrical acoustics (i.e., "facet") component of (3.8) is negligible vis-à-vis the Bragg term, [4]. Accordingly, we choose $\theta_{oT} = 80°$ ($\phi = 10°$) with $\phi_{oT} = \pi/2$, cf. Fig. A.2-1a, and signal frequency $f_o = 1$ kHz. Thus we have the following calculations:

A. Calculations ($\theta_{oT} = 80°$; $f_o = 1$ kHz; $\langle\phi_L^2\rangle^{\frac{1}{2}} = 0° - 50°$)

(1.) $k_o = 2\pi/\lambda_o = 2\pi f_o/c_o = 2\pi\ 10^3/1.5 \cdot 10^3 = 4.188\ (\text{rad m}^{-1})$

$$\therefore k_o^4 = 3.08 \cdot 10^2\ (\text{rad m}^{-1})^4 \qquad (3.20a)$$

(2.) $\theta_{oT} = 80°$: $\therefore \cos\theta_{oT} = 0.174$; $\cos^4\theta_{oT} = 9.09 \cdot 10^{-4}$; $\sin\theta_{oT} = 0.985$

$\tan\theta_{oT} = 5.67$; $\tan^2\theta_{oT} = 3.21 \cdot 10$; $\sin^4\theta_{oT} = 0.941$

$\therefore 2k_o \sin\theta_{oT} = 8.25$ (3.20b)

(3.) From (3.10) and Table 3.2 we get $\overline{R_o^2}$ $\overline{S^2}$ for $\langle\phi_L^2\rangle^{\frac{1}{2}} = 0, 10°, \ldots, 50°$. (3.20c)

(4.) $W_H(0, 2k_o \sin\theta_{oT})$, (2.11b):

$$W_H = \frac{4\pi C_1}{[k_c^2 + (2k_o \sin\theta_{oT})^2]^2}\ ; \quad k_c = 0.05\ \text{m}^{-1}; \quad C_1 = 0.013$$

$$\therefore \quad \doteq \frac{\pi C_1}{4k_o^4 \sin^4\theta_{oT}} = k_o^{-4}\ \frac{\pi(0.013)}{4(0.941)} = k_o^{-4}(1.09 \cdot 10^{-2}). \qquad (3.20d)$$

B. The Backscatter Cross Section, $\hat{\sigma}^{(0)}_{back}$

Combining the numerical results of A above with those in Table 3.2 and applying these, in turn, to Eq. (3.8) for the backscatter cross section, specifically at small grazing angles ($\theta_{oT} = 80°$), gives us the results shown in Table 3.3 following:

Table 3.3 Model Ia--Backscatter Cross Section, $\hat{\sigma}^{(0)}_{inc}$:

$[\theta_{oT} = 80°;\ (\phi_{oT} = \pi/2);\ f_o = 1\ kHz]$

$\langle\phi_L^2\rangle^{1/2}$: rms slope	$\sigma^2_{L(x=y)}$	$\hat{\sigma}^{(0)}_{inc-L}$		$+\ \hat{\sigma}^{(0)}_{inc-H}$	$= \hat{\sigma}^{(0)}_{inc}$
0	0	0	($-\infty$ dB)	$9.99 \cdot 10^{-7}$	(-60.0 dB)
10	$3.11 \cdot 10^{-2}$	$1.27 \cdot 10^{-95}$	(-949 dB)	$1.93 \cdot 10^{-6}$	(-57.2 dB)
20	$1.32 \cdot 10^{-1}$	$2.75 \cdot 10^{-51}$	(-506 dB)	$4.19 \cdot 10^{-6}$	(-53.8 dB)
30	$3.33 \cdot 10^{-1}$	$8.76 \cdot 10^{-20}$	(-191 dB)	$7.37 \cdot 10^{-6}$	(-51.4 dB)
40	$7.04 \cdot 10^{-1}$	$3.81 \cdot 10^{-9}$	(-84.2 dB)	$1.16 \cdot 10^{-5}$	(-49.4 dB)
50	1.42	$1.38 \cdot 10^{-4}$	(-38.6 dB)	$1.73 \cdot 10^{-5}$	(-47.6 dB)
	Eq. (3.14)	Eq. (3.8)		Eq. (3.8) (no Kirchoff correction)	

As expected, the frequency-independent "facet" component, $\hat{\sigma}^{(0)}_{inc-L}$, of $\hat{\sigma}^{(0)}_{inc}$, (3.8), is quite negligible vis-à-vis the Bragg component, $\hat{\sigma}^{(0)}_{inc-H}$, until the rms slopes become large $\langle\phi_L^2\rangle^{1/2} \gtrsim 45°$ (e.g., $\sigma_L^2 \doteq 1$), at 1 kHz specifically. For example, at $\sigma_L^2 = 1.42$ ($\langle\phi_L^2\rangle^{1/2} = 50°$) the facet component actually dominates as shown in Fig. 4.1. Also, because of the general form of the wave number spectrum (2.11b), the Bragg component $\hat{\sigma}^{(0)}_{inc-H}$ is essentially independent of frequency, cf. (3.20d) in (3.8) (provided the effective signal frequency f_o is such that $(2k_o \sin\theta_{oT})^2 >> k_c^2 = (0.05)^2$, cf. (3.20d)). Then, $W_H \doteq 4\pi k_o^{-4} C_1 / \sin^4\theta_{oT}$. Here, at the smaller grazing angles ($\theta_{oT} > 70°$) this means f_o $O(\geq 100$ Hz). The backscatter cross section $\hat{\sigma}^{(0)}_{inc}$ for Model Ia is shown in Figure 4.1 ff. The curves ~~****~~ include a +2.5 dB Kirchoff correction, taken for $\theta_{oT} = 80°$ from Fig. 13 of [19]. This is appropriate for rms (wave) slopes of 13.1° [$\equiv \sigma_L^2 = 5.42\ \ 10^{-2}$, for mean wind speeds of v = 20 knots (= 10 m/sec)], but is probably too large for the larger ice slopes here, since the larger "tilt-factors" reduce the penumbra effects of near-grazing incidence. Thus, the corrected curve for $\hat{\sigma}^{(0)}_{inc-back}$ is a conservative upper limit.

C. Remarks and Conclusions

Our results are not sensitive to the "splitting" frequency f_D (or wave number, $k_D = 2\pi/\lambda_D$), cf. [13]. However, it is reasonable to choose this frequency less than the signal frequency (f_o), in any case such that

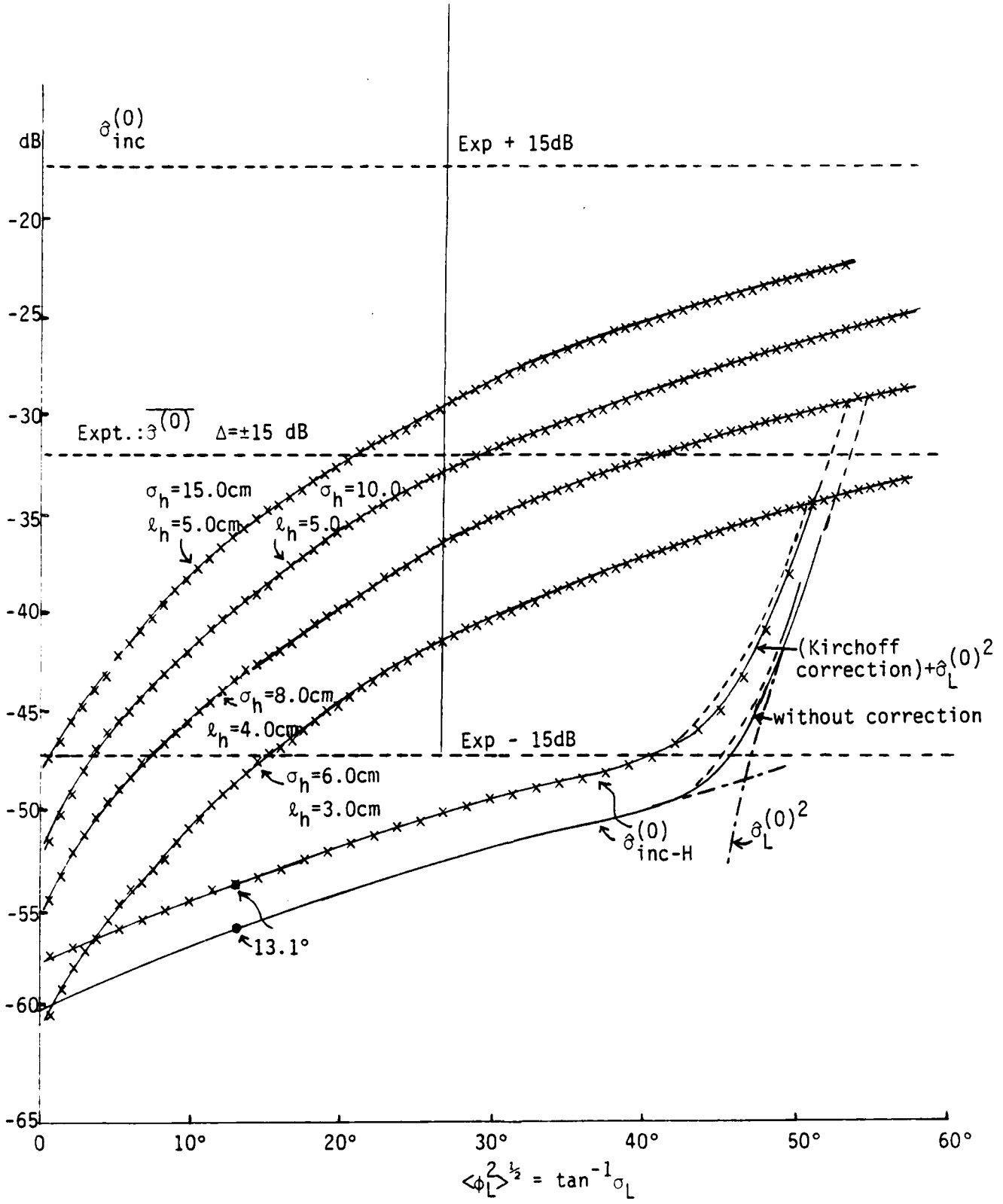

Figure 4.1 Backscatter Cross Sections at $\theta_{OT} = 80°$; f_o = 1 kHz; Model Ib; ×××××××, Eq. (4.5), Model Ia: ×—×—×, Eq. (3.8): $\hat{\sigma}^{(0)}_{inc-h} \pm \hat{\sigma}^{(0)}_{inc}$. (All have Kirchoff correction of +2.5 dB, except ———, Eq. (3.8).)

the Rayleigh number, R_H ($= \sigma_H^2 b_o^2 k_o^2$), for the resulting "high-frequency" Bragg component is small compared to unity, so that the associated perturbational expansion of the Kirchoff model (in the manner of [4]) is valid for obtaining this Bragg contribution. [See the remarks at the beginning of Sec. 3.1.]

The wave number spectrum used for splitting here is given by (2.11b). We calculate σ_H^2, the mean intensity of the Bragg component, from

$$\sigma_H^2 = \int_{k_D}^{\infty} W_H(\underline{k})\underline{dk}/(2\pi)^2 = \int_0^{2\pi} d\phi \, \frac{4\pi C_1}{(k_c^2+k^2)^2} \, \frac{kdk}{(2\pi)^2}$$

$$= \sigma_\zeta^2 \, [1 + (k_D/k_c)^2]^{-1}; \quad \sigma_\zeta^2 = C_1/k_c^2 = 5.68 \text{ m}^2; \quad k_c = 0.05 \text{ rad m}^{-1} . \tag{3.21}$$

Table 3.4 shows $R_H = (\sigma_H b_o k_o)^2$ for various "splitting" wave numbers, k_D, at a signal frequency of 1 kHz and 10° grazing angle, in the backscatter régime, for the Lyon data of Sec. 2.

Table 3.4 Model Ia: R_H @ f_o = 1 kHz, θ_{oT} = 80° (ϕ_{oT} = π/2)

f_D (Hz)	λ_D (m)	k_D = rad m^{-1}	σ_H^2, (3.21) m^2	R_H; $(k_o b_o)^2$=2.116m^{-2}
30	50	0.126	0.772	R_H = 1.63
50	30	0.209	0.307	0.650
100	15	0.419	$7.97 \cdot 10^{-2}$	0.619
200	7.5	0.838	$2.02 \cdot 10^{-2}$	$4.27 \cdot 10^{-2}$
400	3.75	1.68	$5.03 \cdot 10^{-3}$	$1.06 \cdot 10^{-2}$
1 kHz	1.5	4.19	$8.07 \cdot 10^{-4}$	$1.71 \cdot 10^{-3}$
2 kHz	0.75	8.38	$2.02 \cdot 10^{-4}$	$4.27 \cdot 10^{-4}$

For the above geometry (and data) choosing $f_D \geq O(100 \text{ Hz})$ yields a satisfactorily small Rayleigh number ($f_D \leq f_o$-) for the Bragg component. In the present situation, i.e. (3.8) for $\hat{\sigma}_{inc}^{(0)}$, both the "facet" and Bragg components are independent of k_D ($> k_o$).

Conclusion: It is quite apparent from Fig 4.1 and Table 3.1 that the simple, single-surface model (Model Ia), however artificially split to give "facet" and Bragg-scatter contributions, yields too small (incoherent) backscatter cross sections, $\hat{\sigma}_{inc}^{(0)}$, at these comparatively small grazing angles [and intermediate and "high" frequencies, $f_o > O(100\ Hz)$]. Even allowing for the large experimental spreads ($\Delta = O(15\ db)$) in the data (Fig. 4 of [5], and Milne [20], Mellen and Marsh [21]), shown as the dotted line in Fig. 4.1 here for $\theta_{oT} = 80°$, $f_o = 1$ kHz, Model Ia is inadequate to account for the observations.

Accordingly, we must investigate the more complex, two-component surface Model Ib, described in Sec. 2.2 above, to see whether it can reasonably account for the larger obscured backscatter intensities.

Finally, we note that major numerical differences with the analogous ocean wave surface models stem not from the analytical results, cf. (3.8), but from the much larger rms slopes encountered in the ice profiles, as well as from the empirical details of the profile data themselves (cf. Secs. 1, 2).

4. Scattering Cross Sections for Model Ib

As we have seen in Section 3, a single-component, or single-surface model appears to be inadequate to explain the observed (back)scatter cross sections, cf. Fig. 4.1. This strongly suggests that an additional, but independent, small-scale surface structure, riding on the original, larger-scale underice surface may provide the required scattering mechanism, which accounts for the empirical scatter cross sections, particularly at the smaller grazing angles ($\theta_{oT} > 70°$).

4.1 Scattering Cross Sections; Backscatter Cases, Model Ib

Thus, we modify Model Ia, (3.5), according to

$$\boxed{\underline{\zeta}(\underline{r}) = \hat{\underline{i}}_z \zeta_\Lambda + \hat{\underline{n}}_\Lambda \zeta_h} = \hat{\underline{i}}_z(\zeta_L + \zeta_H) + \hat{\underline{n}}_\Lambda \zeta_h \ (= \text{Model Ia} + \hat{\underline{n}}_\Lambda \zeta_h), \quad (4.1)$$

where the additional, small-scale-surface component is $\zeta_h = \zeta_h(\underline{r})$, which is now regarded as normally distributed, $\langle \zeta_h \rangle = 0$, vide Sec. 4.3 ff. The unit normal $\hat{\underline{n}}$, cf. (2.15), reduces to

$$\hat{\underline{n}}_\Lambda \doteq \hat{\underline{n}}_L = \{(\hat{\underline{i}}_x \zeta_x + \hat{\underline{i}}_y \zeta_y - \hat{\underline{i}}_z) \Big/ \sqrt{1 + \zeta_x^2 + \zeta_y^2}\}_L \quad , \qquad \zeta_x \equiv \partial\zeta/\partial x, \quad (4.2)$$

the contribution of the "high-wave number" component, ζ_H, being ignorable vis-à-vis that of ζ_L, in ζ_Λ. [In fact, we recognize (4.1), with $\hat{\underline{n}}_\Lambda \doteq \hat{\underline{n}}_L$, as being formally analogous to our previous ocean wave surface model (2.1)-[4], which includes a soliton or haudraulic jump component riding on the underlying gravity-capillary wind-wave surface. Here, however, ζ_h may be "two-sided," i.e., $\langle \zeta_h \rangle = 0$, unlike the soliton model used in the wind-wave surface study [4], cf. (4.11), (4.12) ff.]

Our analysis here consists of a slightly modified version of the treatment described in [4]. The incoherent scattering cross section may be compactly given by

$$\boxed{\vartheta^{(0)}_{inc} = \{\vartheta^{(0)}_{inc\text{-}L} + \vartheta^{(0)}_{inc\text{-}H}\} + \vartheta^{(0)}_{inc\text{-}h} \ ,} \qquad (4.3)$$

where the first two terms of (4.3) are respectively provided by (3.6) above, in the general bistatic cases, specifically under the Kirchoff conditions described at the beginning of Section 3, which for these classes of profile data are applicable for illuminating frequencies $f_o = O(\gtrsim 50\ Hz)$, viz., the "intermediate" and high frequencies. Specifically, $\vartheta^{(0)}_{inc\text{-}h}$ is given by

$$\vartheta^{(0)}_{inc\text{-}h} = \overline{R_o^2}\ \overline{S^2}\ \frac{k_o^4}{16\pi^2}\, N^{(0)}_{Lh}\ (2\underset{\sim}{\alpha}_o|_{x,y})_{inc}\ W_h(2\underset{\sim}{\alpha}_o|_{x,y}) \ , \qquad (4.4)$$

cf. (2.13)-[4], where W_h is the wave number intensity spectrum of the additional, independent surface component, ζ_h.

For backscatter we use (3.8) for the first two terms of (4.3) and write (4.4), $\Phi_{oT} = \pi/2$, as

To obtain an estimate of the wave number, k_s, at which a new spectrum is required, we solve (A.1-13) or (A.1-13a) for k_s, getting (A.1-14), $K_{Sc} >> 1$. The results are tabulated in Table A.1-1:

Table A.1-1 Spectrum Transition Wave Number

k_s, $C_1 = 0.013$; $k_c = 0.05$ (m^{-1})

$\langle \phi_L^2 \rangle^{1/2}$: rms slope	$\sigma^2_{L(x=y)} = \tan^2 \langle \phi \rangle^{1/2}$	k_s (m^{-1})	$\lambda_s (= 2\pi/k_s)$ (m)
0°	0	0	
10	$3.11 \cdot 10^{-2}$	$\pm$ 0.47	$\pm$ 13.3
20	$1.32 \cdot 10^{-1}$	$2.18 \cdot 10^{3}$	$2.88 \cdot 10^{-3}$
30	$3.33 \cdot 10^{-1}$	$1.10 \cdot 10^{10}$	$5.71 \cdot 10^{-10}$
40	$7.04 \cdot 10^{-1}$		
50	1.42		

Clearly, the transition wave number k_s is much too large for the rms slopes encountered in practice with ice profiles, e.g., O(30°), so that $k_s = O(10^{10})$ or $\lambda_s = O(\frac{1}{2} \cdot 10^{-10}$ m). This supports the argument, developed in the text (esp. Secs. 3, 4) that a true two-component or two-scaled profile surface should be considered, since a single-scaled profile, however artificially split, yields much too small backscatter cross sections (for, in the text, grazing régimes). As we note above, such a profile requires much too short a cut-off wavelength, α_s, to provide the magnitude of rms slopes typically encountered, vide Table A.1-1 above.

A.1-4 Covariance Functions and Wave-Number Spectra (Model Ib)

For our surface elevation model (4.10), when each projection element is independent, so that a poisson model of element location may be applied, [20]-[22], we readily find that the covariance of the profile is given by

$$K_h(\underset{\sim}{\Delta r}) = \int_{\Lambda} \rho(\underset{\sim}{r'}) \langle \zeta(\underset{\sim}{r_1} - \underset{\sim}{r'}, \underset{\sim}{\theta}) \zeta(\underset{\sim}{r_1} + \underset{\sim}{\Delta r} - \underset{\sim}{r'_1}, \underset{\sim}{\theta}) \rangle_{\underset{\sim}{\theta}} \, d\underset{\sim}{r'}, \qquad \text{(A.1-15)}$$

since

$$\frac{\partial \zeta(\underline{r})}{\partial x} = \int_{-\infty}^{\infty} \int (-ik_x) S_\zeta(\underline{k}) \frac{d\underline{k}}{(2\pi)^2} e^{-i\underline{k}\cdot\underline{r}} ,$$

where S_ζ is the amplitude wave-number spectrum of $\zeta(\underline{r})$. Thus, we write

$$\therefore \quad \overline{\left(\frac{\partial \zeta}{\partial x}\right)^2} = \sigma^2_{L(x=y)} = \left[\int_{-\infty}^{\infty} \int k_{x1} k_{x2} \overline{S_\zeta(\underline{k}_1) S_\zeta(\underline{k}_2)^*} e^{-i\underline{k}_1\cdot\underline{r}_1 + i\underline{k}_2\cdot\underline{r}_2} \frac{d\underline{k}_1 d\underline{k}_2}{(2\pi)^2} \right]_{\Delta\underline{r}=0} \tag{A.1-10}$$

and since

$$\overline{S_\zeta(\underline{k}_1) S_\zeta(\underline{k}_2)^*} = (2\pi)^2 \delta(\underline{k}_2 - \underline{k}_1) W_2(\underline{k}_1)_\zeta, \qquad \text{with } \Delta\underline{r} = \underline{r}_2 - \underline{r}_1, \tag{A.1-11}$$

which defines the wave number spectrum <u>intensity</u> W_2, we use $k^2 = k_x^2 + k_y^2 = 2k^2_{x=y}$ and (A.1-11) directly to obtain the result (A.1-9). Equivalently, for these isotropic cases

$$2\sigma^2_{L(x=y)} = \overline{\left(\frac{\partial \zeta}{\partial x}\right)^2} + \overline{\left(\frac{\partial \zeta}{\partial y}\right)^2} = \int_{-\infty}^{\infty} \int k^2 W_2(\underline{k}) \frac{d\underline{k}}{(2\pi)^2} = \frac{1}{2\pi} \int_0^{\infty} k^3 dk W_2(k). \tag{A.1-12}$$

Now, using (A.1-7) in (A.1-9) and truncating the spectrum W_2 at some (large) spectrum transition wavenumber k_S, to get a finite rms slope, we have here

$$\sigma^2_{L(x=y)} = C_1 \int_0^{k_S} \frac{k^3 dk}{(k_c^2 + k^2)^2} = \frac{C_1}{2} \left\{ \log(K_{Sc}^2 + 1) + \frac{1}{1 + K_{Sc}^2} - 1 \right\}, \quad K_{Sc} \equiv \frac{k_S}{k_c}, \tag{A.1-13}$$

$$= \frac{C_1}{2} (2 \log K_{Sc} - 1), \quad K_{Sc} \gg 1, \tag{A.1-13a}$$

with

$$\therefore \quad k_S = k_c \exp\{\tfrac{1}{2} [1 + 2\sigma^2_{L(x=y)}/C_1]\} . \tag{A.1-14}$$

from Watson [10], p. 410, (2), with

$$W_2(\underset{\sim}{k})_{\text{Mellen}} = 2C_1/(k_c^2+k^2)^2 \ , \quad \text{cf. (4) of [5].} \tag{A.1-7a}$$

Similarly, using (A.1-7) in (A.1-5a) gives the correct covariance, viz.:

$$\sigma_\zeta^2 \rho_\zeta(\underset{\sim}{\Delta r}) = \frac{1}{(2\pi)^2} \int_{-\infty}^{\infty} \int \frac{4\pi C_1}{(k_c^2+k^2)^2} e^{ik\Delta r \cos\phi} dk_x dk_y$$

$$= \frac{1}{(2\pi)^2} \int_0^{2\pi} d\phi \int_0^{\infty} kdk e^{ik\Delta r \cos\phi} \frac{4\pi C_1}{(k_c^2+k^2)^2}$$

$$= 2C_1 \int_0^{\infty} \frac{J_0(k\Delta r)kdk}{(k_c^2+k^2)^2} = \left(\frac{C_1}{k_c^2}\right) k_c \Delta r K_1(k_c \Delta r), \tag{A.1-8}$$

as required, cf. Watson [10], p. 434, (2).

A.1-3 RMS Slopes (Model Ia)

The calculation of rms slopes $\sigma_{L(x=y)}$ of the ice profile can readily be carried out once the spectrum (or the correlation function) is known. From (A.1-4), or (A.1-8), it is at once evident that with this spectrum model $\sigma^2_{L(x=y)}$ becomes infinite, so that for suitably small wave numbers the empirical spectrum clearly is inadequate, i.e., does not fall off fast enough as $k \to \infty$. Thus, we may use the empirical spectrum (A.1-7) up to some effective cut-off frequency k_s, at which point another spectral law takes over. Just what the new spectrum (at $k > k_s$) is remains to be determined by experiment [cf. our remarks à propos of Model Ib, Sec. 4].

For the (isotropic) slopes we have, in general,

$$\boxed{\sigma^2_{L(x=y)} = \overline{\left(\frac{\partial \zeta}{\partial (x=y)}\right)^2}\Bigg|_{\underset{\sim}{\Delta r}=0} = \frac{1}{4\pi} \int_0^{\infty} kdk \cdot k^2 W_2(\underset{\sim}{k}) \ ,} \tag{A.1-9}$$

and since $\lim_{x\to 0} xK_1(x) = 1$, we have at once (cf. Watson, [10], p. 185):

$$\left.\begin{aligned} &\boxed{\sigma_\zeta^2 = C_1/k_c^2} = 0.013/(0.05)^2 = 5.20\ (m^2);\ \therefore \sigma_\zeta = 2.28 [\simeq 2.38 \simeq \hat{\sigma}_\zeta,\ (2.6)] \\ &\therefore\ \boxed{\rho_\zeta(\Delta r) = k_c \Delta r K_1(k_c \Delta r),} \end{aligned}\right\} \quad (A.1\text{-}4)$$

which is Eq. (2.10b).

A.1-2 (Isotropic) Two-Dimensional Cases (Model Ia)

For the associated spectra and correlation function in the two-dimensional cases we have, generally,

$$\underline{(2\text{-dimensions})}: \quad K_\zeta(\underset{\sim}{\Delta r}) = \sigma_\zeta^2 \rho_\zeta(\underset{\sim}{\Delta r}) = \int_{-\infty}^{\infty} \int W_2(\underset{\sim}{k}) e^{-i\underset{\sim}{k}\cdot\underset{\sim}{\Delta r}} \frac{dk}{(2\pi)^2}, \quad (A.1\text{-}5a)$$

with

$$W_2(\underset{\sim}{k}) = \int_{-\infty}^{\infty} \int K_\zeta(\underset{\sim}{\Delta r}) e^{i\underset{\sim}{k}\cdot\underset{\sim}{\Delta r}}\, d(\underset{\sim}{\Delta r}). \quad (A.1\text{-}5b)$$

Similar to (A.1-2) there is the relation

$$2\pi W_2(k)_{\text{Mellen,[5]}} = W_2(\underset{\sim}{k}). \quad (A.1\text{-}6)$$

Let us use (A.1-3) and the postulated isotropic character of the wave number spectrum to determine the two-dimensional form of $W_2(\underset{\sim}{k})$ here, viz. (2.11b). From (A.1-5b) we have

$$\begin{aligned} W_2(\underset{\sim}{k}) &= \int_0^2 d\phi \int_0^\infty \Delta r\, d(\Delta r) \sigma_\zeta^2 (k_c \Delta r) K_1(k_c \Delta r) e^{i\Delta r k \cos\phi} \\ &= 2\pi\sigma_\zeta^2 \int_0^\infty \Delta r J_0(k\Delta r) K_1(k_c \Delta r)(k_c \Delta r) d(\Delta r) \\ &= (2\pi\sigma_\zeta^2/k_c^2) \int_0^\infty J_0(kx) K_1(x) x^2 dx, \qquad b \equiv k/k_c, \end{aligned}$$

$$\therefore\ \boxed{W_2(\underset{\sim}{k}) = \frac{4\pi C_1}{(k_c^2 + k^2)^2}},\quad 0 \leqslant \phi \leqslant 2\ ;\quad k = \sqrt{k_x^2 + k_y^2},\ \text{Eq. (2.11b)}, \quad (A.1\text{-}7)$$

Appendix A.1. Wave Number Spectra and Spatial Correlation Functions. Models Ia, Ib

A.1-1 One-Dimensional Correlation Functions and Spectra (Model Ia)

For the wave number spectrum and associated spatial correlation function we employ the following Fourier transform relations:

$$\underline{\text{(1-dimension)}}: \quad K_\zeta(|\underline{\Delta r}|) \equiv \sigma_\zeta^2 \rho_\zeta(|\underline{\Delta r}|) = \int_{-\infty}^{\infty} W_1(k) e^{-ik\Delta r} \frac{dk}{2\pi}, \quad \Delta r = |\underline{\Delta r}|, \tag{A.1-1a}$$

with

$$W_1(k) = \int_{-\infty}^{\infty} K_\zeta(\underline{\Delta r}) e^{ik\Delta r} d(\Delta r), \tag{A.1-1b}$$

where

$$\sigma_\zeta^2 = K_\zeta(0) = \int_{-\infty}^{\infty} W_1(k) \frac{dk}{2\pi} \tag{A.1-1c}$$

for the mean intensity of the profile elevation, ζ. In reference [5] the wave number intensity spectrum is defined as

$$2\pi W_1(k)_{\text{Mellen,[5]}} = W_1(k) \tag{A.1-2}$$

here.

It is instructive to obtain $K_\zeta(\Delta r)$ from the empirical fit of Mellen et al. [5], (2.9) viz.

$$W_1(k) = \pi C_1/(k_c^2 + k^2)^{3/2} . \tag{A.1-3}$$

Thus, using (A.1-3) in (A.1-1a) gives*

$$\sigma_\zeta^2 \rho_\zeta(\Delta r) = \int_{-\infty}^{\infty} \frac{\pi C_1}{(k_c^2+k^2)^{3/2}} \frac{dk}{2\pi} e^{-ik\Delta r} = C_1 \int_0^{\infty} \frac{\cos k\Delta r}{(k_c^2+k^2)^{3/2}} dk = \frac{C_1}{k_c^2}(k_c\Delta r) K_1(k_c\Delta r), \tag{A.1-3a}$$

---

*In equation (2) of [5] "constant" should be replaced by "(1/2) constant." This also insures that (4) of [5] agrees with (2.11b), etc.

(i). To include specific keel structures in the manner of Models IIa,b (Sec. 2.2);

(ii). To compare the results of (i) with those of the present study;

(iii). To evaluate forward, as well as backscatter, including coherent scatter components.

Critically needed now are active experimental data, both linear and directional, at wavelengths O(6 m - 1 cm) on underice profiles for typical regions in the ocean. With such data we can evaluate and compare the various scattering models, and select the one appropriate to the profile régime in question.

present results depend primarily on the chosen parameter values of the model in question, and only secondarily on the specific analytic structure.

The conditions under which our quantitative models above have been constructed and evaluated are, concisely:

Model Conditions

(1). Far-field operations, for both source and receiver vis-à-vis the underice bottom (Appendix A.2);

(2). Kirchoff-Bragg scatter conditions (Sec. 3), requiring "intermediate" O(0.10-1.0 kHz), and "high" frequencies O(≥ 1.0 kHz), which are in the large Rayleigh number regimes;

(3). Composite gaussian surface profile model (Secs. 2, 2.1), based on Lyon's data [1] (but see Sec. 2.1 for limitations);

(4). An isotropic covariance (and associated wave-number spectra) for the large-scale profile component, based on Mellen et al.'s recent work [5];

(5). Finite (rms) slopes--Sec. 3.3 C; gaussian pdf of slopes;

(6). "Single-bounce" geometry for ice, source, and receiver; and $\nabla c = 0$;

(7). "Hard" ice boundary, with local plane wave reflection coefficient (R_0=1), cf. Sec. 3.2, A.

(8). Large "tilt-factors" and non-negligible shadowing corrections, Sec. 3.2, 4.2.

(For details, see the text above and Appendixes A.1, A.2). Unlike the related problems of scattering from the ocean wave surface [4], [12], the surface slopes involved here are much larger, O(2.5-3), with consequent modification of the analytical and numerical results, cf. Secs. 3.2 B, C; 4.2, Table 3.2 above.

Our Models Ia, Ib do not explicitly designate a keel structure, for the reasons we have already noted in Section 1. Neither are we concerned here with "low"-frequency scatter [f_0 = O(≤ 30-50 Hz)], and multiple surface interactions, produced by suitable geometries in a non-zero gradient ocean ($\nabla c \neq 0$). These, and other model situations, are reserved to subsequent studies. Of these, our immediate next steps are

is not critical; rather, it is the values of height ($\sim\sigma_h$) and scale ($\sim\ell_h$) which are significant (except, of course, at the very high wave numbers, which influence the (rms) slopes).

5. Concluding Remarks

The principal general results of this study are:

I. Determination of the incoherent (backscattering) cross section, $\hat{\sigma}^{(0)}_{inc}$, for Model Ia: a single (isotropic) underice surface (Sec. 2, Sec. 3);

II. Extension of Model Ia to Model Ib, which adds an additional surface component, of much smaller scale.

The general result II is generated from the observation that

III. Model Ia is shown to be inadequate to account for the empirically observed backscatter cross sections (Fig. 4.1), particularly in the critical régimes of small grazing angles ($\theta_{oT} > 70°$) and "high" frequencies $f_o \geq O(0.5\ kHz)$. Furthermore, Model Ia, if applied for all wave numbers, yields infinite (rms) slopes (Sec. 3.3 C).

IV. Model Ib can account for the observed (back)scatter data, cf. Fig. 4.1. The scale of the added independent surface component, ζ_h, appears to be: rms elevation $\sigma_h = O(8 - 15\ cm)$; e^{-1}-correlation distance $\ell_c = O(4\text{-}7\ cm)$. (Model Ib always has finite rms slopes.)

V. These models and results strongly support the need for profile data at wavelengths O(6m - 1 cm), from which appropriate wave number spectra can be constructed for model use.

Accordingly, a two-, independent-component model of the (underice) profile, involving small- and large-scale surface elements, can account for the observed (back)scatter cross sections, particularly in the limiting régimes of "high" frequencies and small grazing angles. Whether such a model (Model Ib here) is appropriate, i.e., adequately represents the underice scattering mechanisms involved, remains to be determined, both theoretically and empirically [the latter from V above, and remarks below: "next steps"]. One limitation here is the restriction of ζ_Λ, (4.1), to a single gauss process, albeit with the correct (i.e., empirical) second moments, as described in Sec. 2.1 above. Models II [Secs. 2.2-2.4] are not so constrained. It is emphasized, also, that the

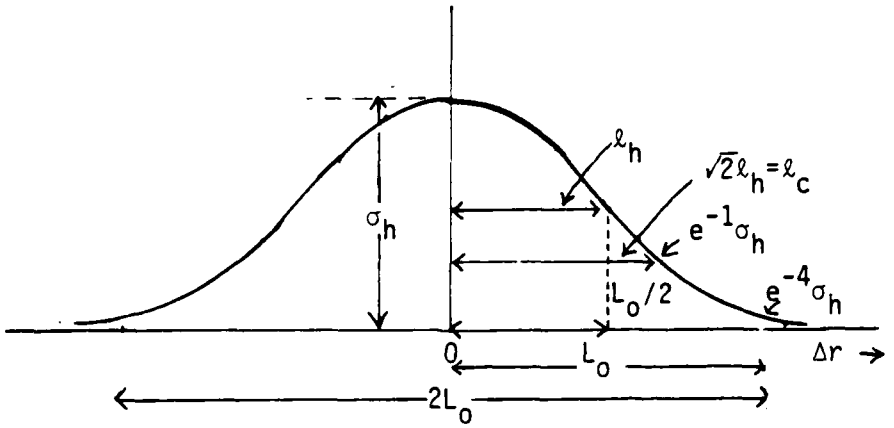

Figure 4.2 Sketch of $K_h(\underset{\sim}{\Delta r})$, Eqs. (4.12), (4.12a); ℓ_c = "correlation distance," $K_h = e^{-1}\sigma_h$.

Remarks

Figure 4.1 shows the incoherent backscatter cross section $\hat{\sigma}^{(0)}_{\text{inc-h}}$, attributable to the small-scale component riding on the large-scale profile, ζ_S, for a selection of parameter values (σ_h, ℓ_h). We have chosen values which give cross sections in the range of empirical values when the rms slope is $O(30°)$. *Typical values are* $\sigma_h = O(10\ cm)$ *and* $\ell_h = O(4\text{-}5\ cm)$, or $\ell_c = (5+ - 7\ cm)$, for our present model. Here $\hat{\sigma}^{(0)}_{\text{inc-back}} \triangleq \sigma^{(0)}_{\text{inc-h}}$ for slopes $O(20° - 45°)$: the independent, "small-scale" component riding on the large-scale profile is here clearly the dominant contributor to the incoherent backscatter cross section, for these (comparatively) small grazing angles and high frequencies, $O(f_o = 1\ kHz)$. The rms roughness of ζ_h, as measured by σ_h, is $O(2\text{-}5\%)$ of that of the (composite) large-scale profile, ζ_Λ. [Of course, at this stage we do not have experimental verifications of the scale of these numbers, except indirectly through the postulate of Model Ib and the comparisons shown in Fig. 4.1.]

Finally, if we use the generalized version, (A.1-22), of the wave-number spectrum noted above (4.14), we obtain for the same parameters (and $\partial_\ell = \sqrt{\pi/2}\ \ell_h$) essentially the same values of $\hat{\sigma}^{(0)}_{\text{inc-h}}$, more precisely, values only $O(2.5\text{-}3.0\ db)$ lower than those shown in Fig. 4.1. This is in keeping with our remark above (beginning of Sec. 4.3) that the "shape" of the individual projections forming the small-scale surface component

4.4 Model Ib. A Numerical Example:
Backscatter @ $\theta_{oT}=80°$, $\phi_{oT}=\pi/2$; $f_o=1$ kHz

Combining (4.7) for $N_{Lh}^{(0)}$ cf. Table 3.2, (4.14) for $W_h(0,2k_o\sin\theta_{oT})$; $\overline{R_o^2}$, (3.10) and $\overline{S^2}$, Table 3.2, in (4.5) gives us the desired quantitative structure for the backscatter cross section $\hat{\sigma}_{inc-h}^{(0)}$, arising from the added surface mechanisms, ζ_h. Table 4.1 shows a range of values of $\hat{\sigma}_{inc-h}^{(0)}$, for various choices of model parameters

Table 4.1 Model Ib--Backscatter Cross Section
$\hat{\sigma}_{inc-h}^{(0)}$, Eq. (4.5): (Uncorrected*)
[θ_{oT} = 80°; f_o = 1 kHz; (ϕ_{oT} = π/2)]

$\langle\phi^2\rangle^{1/2}$: rms slope	ℓ_h = 3.0 cm, σ_h = 3.0 cm	6.0	9.0	ℓ_h = 4.0 cm, σ_h = 4.0 cm	8.0	12.0	ℓ_h = 5.0 cm, σ_h = 5.0 cm	10.0	15.0
0	-68.6 (db)	-62.6	-59.1	-63.7	-57.7	-54.2	-60.0	-54.0	-50.5
10	-58.4	-52.4	-48.9	-53.5	-47.5	-44.0	-49.8	-43.8	-40.3
20	-52.8	-46.8	-43.3	-47.9	-41.9	-38.4	-44.2	-38.2	-34.7
30	-48.4	-42.4	-38.9	-43.5	-37.5	-34.0	-39.8	-33.8	-30.3
40	-45.6	-39.6	-36.1	-40.7	-34.7	-31.2	-37.0	-31.0	-27.5
50	-43.2	-37.2	-33.1	-38.3	-32.3	-28.8	-34.6	-28.6	-25.1

*We add a nominal +2.5 db to each entry, to provide the needed correction for the Kirchoff approximation at ϕ_{oT} = 80° (¢=10°), from Fig. 13 of [19]; cf. Fig. 4.1.

The shaded regions of the Table indicate cross-sectional values that fall within the Δ-region (±15 db) of uncertainty in the empirical data shown in Fig. 4.1. Also in Fig. 4.1 are four curves, representative of possible model values (Model Ib). (The Δ-region is -17 to -47 db.)

Figure 4.2 shows $K_h(\underline{\Delta r})$ and typical parameter relations: in our present model L_o, and therefore ℓ_h, ℓ_c are fixed; (for a model in which L_o (= $2\ell_h$) is random, see Appendix A.1-4). Here ℓ_c (= $\sqrt{2}\ell_h$) is the correlation distance of the profile component (ζ_h).

cf. Appendix A.1-4, with

$$\sigma_h^2 \equiv K_h(0) = \gamma_o \overline{\zeta_o^2}\, L_o^2\pi/8; \qquad \ell_h = L_o/2\ ; \quad \Delta r^2 = (\Delta x)^2 + (\Delta y)^2, \tag{4.12a}$$

where the mean value is explicitly

$$\langle \zeta_h \rangle = \gamma_o \overline{\zeta_o}\, L_o^2\pi/4\ . \tag{4.12b}$$

(Note that if $\overline{\zeta_o} = 0$: the mean "bump" height is zero, then there is no "dc"-component in the wave number spectrum, cf. (4.15) ff.) Equation (4.12) is shown in Fig. 4.2. (However, for an alternative model, extending (4.12), see Cases I,II in Appendix A.1-4, and closing remarks in this Section.)

The two-dimensional wave number spectrum corresponding to (4.12) is obtained from

$$W_h(\underline{k}) = \int_{-\infty}^{\infty}\int K_h(\underline{\Delta r})e^{i\underline{k}\cdot\underline{\Delta r}}\, d(\underline{\Delta r}), \tag{4.13}$$

cf. (A.1-5b). We have, for $\underline{k} = (0, 2k_o \sin\theta_{oT})$ specifically here

$$\boxed{W_h(\underline{k}) = 2\pi\sigma_h^2\ell_h^2 e^{-2(k_o\ell_h\sin\theta_{oT})^2}} \tag{4.14}$$

for the "continuum" part of the spectrum. If $\overline{\zeta}_o > 0$, then the complete wave number spectrum is

$$\hat{W}_h(\underline{k}) = \gamma_o^2\, \overline{\zeta_o}^2\, \frac{\pi^3}{4}\, L_o^4 \underline{\delta}(\underline{k}-0) + 2\pi\sigma_h^2\ell_h^2 e^{-2(k_o\ell_h\sin\theta_{oT})^2}\ , \tag{4.15}$$

where $\underline{\delta}(\underline{k}-0) = \delta(k_x-0)\delta(k_y-0)$ and $\int_{-\infty}^{\infty} Ae^{ik_x\Delta x}\, d(\Delta x) = 2\pi A\delta(k_x-0)$, etc.

(Note, incidentally, that ζ_h has finite rms slopes, unlike ζ_s above; (Appendix A.1). The "dc"-component in (4.15) does not, of course, influence the scattered radiation.

given by the results of Table 3.2 and Fig. 3.1, cf. Sec. 3.2, C. The dominant effect, however, here is that produced by the "tilt," embodied in $N^{(0)}_{Lh\text{-}inc}$, cf. (4.9).

4.3 Model of the Small-Scale, Additive Surface Component, ζ_h

A variety of plausible models for the small-scale component ζ_h is certainly available at this stage of our study. One such model, which we employ here, is that involving random "bumps" or projections, distributed in space independently, riding on the large-scale surface, ζ_s, cf. (4.1). These projections are accordingly poisson distributed, and may overlap, or ride upon each other occasionally. Physically, these "bumps" represent inhomogeneities in the local crystal formations on the large-scale surface, produced by near-surface freezing forces.

A reasonable model of a typical ($j^{\underline{th}}$) projection is given by the gaussian form

$$\zeta_{h_j} \equiv \zeta_h(\underline{r},\underline{r}_j) = \zeta_o e^{-4|\underline{r}-\underline{r}_j|^2/L_o^2} , \tag{4.10}$$

where $\underline{r}_j$ is a (random) location (referred to the reference plane, S_o, cf. Figs. A.2-1, A.2-2). [What is primarily important in such models is the height ($\sim\zeta_o$) and spread ($\sim L_o$); the actual spatial shape only becomes critical out on the "tails" ($|\underline{r}-\underline{r}_j| >> L_o$), or equivalently, for the high wave-number fall off of the associated spectrum.] Accordingly, for the isotropic poisson process ζ_h (4.10), we may write (cf. Appendix A.1-4) for the mean and covariance, respectively, generally

$$\langle\zeta_h\rangle = \gamma_o\langle\zeta_h(\underline{r}_1)\rangle \; ; \quad K_h(\underline{\Delta r}) = \gamma_o\langle\zeta_h(\underline{r}_1)\zeta_h(\underline{r}_1+\underline{\Delta r})\rangle , \tag{4.11}$$

where γ_o is the process density (in space) = <u>average number of "bumps" per unit area</u> (on ζ_Λ) cf. [20], [21].

For our specific isotropic model (4.10), (4.11) reduces to

$$\boxed{K_h(\underline{\Delta r}) = \frac{\gamma_o \pi L_o^2 \overline{\zeta_o^2}}{8} e^{-2\Delta r^2/L_o^2} \equiv \sigma_h^2 e^{-\Delta r^2/2\ell_h^2}} , \tag{4.12}$$

$$\boxed{N^{(0)}_{\substack{\text{Lh-inc}\\ \text{back}}}\Big|_{\theta_{oT}=\pi/2} = 16\,\{I^{(4)}\sin^4\theta_{oT} + 6I^{(2)}\sin^2\theta_{oT}\cos^2\theta_{oT} + I^{(0)}\cos^4\theta_{oT}\},} \tag{4.7}$$

where

$$I^{(0)}(a) \equiv \int_{-\infty}^{\infty}\int \frac{e^{-(x^2+y^2)/2\sigma^2_{(x=y)}}}{1+x^2+y^2}\,\frac{dxdy}{2\pi\sigma^2_{(x=y)}} = -a^2e^{a^2}\,Ei(-a^2);\ a^2 \equiv 1/2\sigma^2_{(x=y)}; \tag{4.8a}$$

$$I^{(2)}(a) \equiv \int_{-\infty}^{\infty}\int \frac{(x^2 \text{ or } y^2)e^{-(x^2+y^2)/2\sigma^2_x}}{1+x^2+y^2}\,\frac{dxdy}{2\pi\sigma^2_x} = \frac{1}{2}\,\{1 - I^{(0)}(a)\},\ \text{cf. (3.17)}, \tag{4.8b}$$

$$I^{(4)}(a) \equiv \int_{-\infty}^{\infty}\int \frac{(x^4 \text{ or } y^4)e^{-(x^2+y^2)/2\sigma^2_x}}{1+x^2+y^2}\,\frac{dxdy}{2\pi\sigma^2_x} = \frac{3}{8}\left\{\frac{1}{a^2} - 2I^{(2)}(a)\right\}$$

$$= \frac{3}{8}\left\{\frac{1}{a^2} - 1 + I^{(0)}(a)\right\}, \tag{4.8c}$$

and Ei(x) is the (tabulated) exponential integral, [17], [18]. (Note that with vanishing slopes, $a \to \infty$, $I^{(0)} \to 1$, and $I^{(2)}$, $I^{(4)} \to 0$.) The result (4.7) is, in the general bistatic cases (with $\phi_{oT} = \pi/2$):

$$\boxed{\frac{N^{(0)}_{\text{Lh-inc}}}{16}\Big|_{\theta_{oT}=\pi/2} = \left\{\alpha^4_{oy}I^{(4)}(a) + 6\alpha^2_{oy}\alpha^2_{oz}I^{(2)}(a) + \alpha^4_{oz}I^{(0)}(a)\right\},} \tag{4.9}$$

cf. (7.33e)-[4], and (A.2-11), (A.2-13, 14) for α_{ox}, α_{oy}, α_{oz}, etc. Values of $N^{(0)}_{\text{Lh-inc}}/16$ for the backscatter cases are tabulated in Table 3.2 and shown in Fig. 3.1. This tilt-factor is seen to be much larger than $N^{(0)}_{\text{LH-inc}}/16$, for the artificially "factored" surface $\zeta_\Lambda = \zeta_L + \zeta_H$, cf. Sec. 3.1 et seq., as the profile slopes increase.

The other factors which scale $\hat{\sigma}^{(0)}_{\text{inc}}$ remain unchanged in basic structure: $\overline{R^2_o}$ = 0 db, cf. (3.10), and the shadowing factor, $\overline{S^2}$, is still

$$\hat{\sigma}^{(0)}_{\text{inc-h}}\Big|_{\substack{\text{back}\\ R_\zeta >> 1\\ \phi_{oT}=\pi/2}} = \overline{R_o^2}\;\overline{S^2}\;\frac{k_o^4}{16\pi^2}\,N^{(0)}_{Lh}(\theta_{oT})\Big|_{(\text{back})}^{(\text{inc})}\,W_h(0,2k_o\sin\theta_{oT}). \tag{4.5}$$

As before, cf. (2.14a)-[4], $N^{(0)}_{Lh}$ is the "tilt-factor" for ζ_h, associated with the larger-scale surface component ζ_L, and is given generally by

$$N^{(0)}_{Lh\text{-inc}} = 16\left\langle \frac{(\alpha_{ox}\zeta_x + \alpha_{oy}\zeta_y - \alpha_{oz})^4}{1+\zeta_x^2+\zeta_y^2}\right\rangle_L , \tag{4.6a}$$

so that for <u>backscatter</u> (with $\phi_{oT} = \pi/2$),

$$N^{(0)}_{Lh-}\Big|_{\text{back}}^{\text{inc}} = 16\left\{\sin^4\theta_{oT}\left\langle\frac{\zeta_y^4}{1+\zeta_x^2+\zeta_y^2}\right\rangle_L + 6\sin^2\theta_{oT}\cos^2\theta_{oT}\left\langle\frac{\zeta_y^2}{1+\zeta_x^2+\zeta_y^2}\right\rangle_L\right.$$

$$\left. + \cos^4\theta_{oT}\left\langle\frac{1}{1+\zeta_x^2+\zeta_y^2}\right\rangle_L\right\} \tag{4.6b}$$

(for symmetrically distributed slopes, about $\langle\zeta_{x,y}\rangle_L = 0$), where (3.15) governs the distribution of ζ_{Lx}, ζ_{Ly} here. As for the Bragg component [$\hat{\sigma}^{(0)}_{\text{inc-H}}$ in (4.3)], the pertinent surface statistics for the new component, $\hat{\sigma}^{(0)}_{\text{inc-h}}$ (4.5), are the wave-number intensity spectrum: there is no requirement that ζ_h in (4.1) be normal, for example.

Finally, the complete expression for $\sigma^{(0)}_{\text{inc}}$ is provided by (3.6) and (4.4), generally, and (3.8) and (4.5) for the backscatter cases treated quantitatively here.

4.2 The Tilt-Factor $N^{(0)}_{Lh\text{-inc-back}}$

Again [cf. <u>B</u>, Sec. 3.2], because of the large rms slopes involved, we must use the exact relations (7.64)-[4], (7.65) -[4] to evaluate (4.6b), with the help of (3.15), (3.17). For the assumed isotropic surfaces here ($\sigma_{Lx} = \sigma_{Ly}$) (4.6b) becomes

where $\underset{\sim}{\theta} = (\zeta_o, \ldots)$, i.e., all statistical parameters of ζ, and Λ is the domain (i.e., surface) over which the individual projections can occur (in our model, individual "bumps" or projections can overlap). On the assumption of a uniform density of "bumps," (4.10), on Λ, we can rewrite (A.1-15) as

$$K_h(\underset{\sim}{\Delta r}) = \gamma_o \int_{\Lambda} \langle \zeta(\underset{\sim}{\lambda},\underset{\sim}{\theta})\zeta(\underset{\sim}{\lambda}+\underset{\sim}{\Delta r},\underset{\sim}{\theta}) \rangle_{\underset{\sim}{\theta}} \, d\underset{\sim}{\lambda} \qquad \text{(A.1-16a)}$$

$$= \gamma_o \overline{\zeta_o^2} \int_{-}^{\infty} \int d\lambda_x d\lambda_y \left\langle e^{-4(\lambda_x^2+\lambda_y^2)/L_o^2 - 4(\lambda_x^2+2\Delta_x\lambda x+\lambda_y^2+2\lambda_y\Delta y+\Delta x^2+\Delta y^2)/L_o^2} \right\rangle_{L_o} \qquad \text{(A.1-16b)}$$

for these isotropic cases. Evaluating (A.1-16b) is straightforward. We get here

$$K_h(\Delta r) = \gamma_o \overline{\zeta_o^2} \left\langle \frac{L_o^2 \pi}{8} e^{-2\Delta r^2/L_o^2} \right\rangle_{L_o} = \left(\gamma_o \overline{\zeta_o^2} \frac{L_o^2 \pi}{8}\right) e^{-2\Delta r^2/L_o^2}, \qquad \text{(A.1-17)}$$

where in our present model we now assume that $w_1(L_o) = \delta(L_o - L_o)$, so that (4.12) is the result.

However, it is instructive to consider some other pdf's of L_o:

Case I: $w_1(L_o)$ = Rayleigh pdf

Here L_o, or ℓ_h, is assumed to be governed by a Rayleigh pdf, viz.:

$$w_1(L_o) = \frac{L_o e^{-L_o^2/2\sigma_\ell^2}}{\sigma_\ell^2}, \quad L_o \geq 0; \quad \underline{\text{or}} \; w_1(\ell_h) = \frac{\ell_h e^{-\ell_h^2/2\sigma_\ell^2}}{\sigma_\ell^2} \qquad \text{(A.1-18)}$$

$$L_o = 2\ell_h$$

Using

$$\int_0^{\infty} x^{\nu-1} e^{-\beta x^{-p} - \gamma x^{-p}} dx = \frac{2}{p} \left(\frac{\gamma}{\beta}\right)^{\nu/2p} K_{\frac{\nu}{\beta}} (2\sqrt{\beta\gamma}), \quad \mathrm{Re}(\beta,\gamma > 0) \qquad \text{(A.1-19)}$$

[23], p. 342, No. 3.478-(4), we see that (A.1-17) becomes, with (A.1-18),

$$K_h(\underset{\sim}{\Delta r}) = \gamma_o \overline{\zeta_o^2}\, \frac{\pi}{2} \int_0^\infty \ell_h^3 e^{-\ell_h^2/2\sigma_\ell^2 - \Delta r^2/2\ell_h^2}\, d\ell_h/\sigma_\ell^2$$

$$\therefore \quad \boxed{K_h(\underset{\sim}{\Delta r}) = (\gamma_o \overline{\zeta_o^2} \pi \sigma_\ell^2) \left\{ \frac{1}{2} \left(\frac{\Delta r}{\sigma_\ell}\right)^2 K_2(\Delta r/\sigma_\ell) \right\},} \qquad \text{(A.1-20)}$$

and since $\lim_{x \to 0} \frac{1}{2} x^2 K_2(x) = 1$, we have directly

$$\boxed{K_h(0) = \gamma_o \overline{\zeta_o^2} \pi \sigma_\ell^2 \equiv \sigma_h^2} \; ; \quad (\sigma_\ell^2 \equiv \overline{\ell_h^2} - \overline{\ell}_h^2) \; . \qquad \text{(A.1-20a)}$$

The associated (two-dimensional) wave-number spectrum from (A.1-5) is now

$$W_2(\underset{\sim}{k}) = \tfrac{1}{2} \sigma_h^2 \sigma_\ell^2 \int_0^\infty x^3 K_2(x) J_0(k\sigma_\ell x) dx, \quad \Delta r/\sigma_\ell \equiv x, \qquad \text{(A.1-21)}$$

$$\therefore \quad \boxed{W_2(\underset{\sim}{k}) = \sigma_h^2 \sigma_\ell^2 4/[1+(k\sigma_\ell)^2]^3 = 4\sigma_h^2 k_\ell^4/(k_\ell^2+k^2)^3, \quad (= W_2(k)) \quad ; \quad k_\ell \equiv 1/\sigma_\ell \; ,} \qquad \text{(A.1-22)}$$

by [10], p. 410, Eq. (2). Unlike the empirical model (A.1-7), this spectrum supports a finite rms slope. From (A.1-12) we see that specifically

$$\sigma^2_{h(x=y)} = \frac{1}{4\pi} \int_0^\infty k^3 W_2(k) dk = \frac{\sigma_h^2 \ell^4}{\pi} \int_0^\infty \frac{k^3 dk}{(k_\ell^2+k^2)^3} = \sigma_h^2 \frac{k_\ell^2}{4\pi} \; (= \sigma_h^2/4\pi\sigma_\ell^2), \qquad \text{(A.1-23)}$$

this last from [23], p. 293, 3.241-(4) directly.

Incidentally, it is <u>not</u> possible to get the covariance (A.1-3,4) from our gaussian model (4.10), as this would require a pdf of ℓ_h of the form

$$w_1(\ell_h) = \ell_h^{-1} \frac{e^{-\ell_h^2/2\sigma_\ell^2}}{\sigma^2} \quad , \quad \ell_h > 0, \tag{A.1-24}$$

which is singular, i.e., not bounded or normalizeable.

Case II: $w_1(L_o)$ = "one-half" Gauss pdf

In this case L_o, or ℓ_h is now assumed to obey a "half-gauss" pdf, viz.:

$$w_1(L_o) = \sqrt{\frac{2}{\pi}} \frac{1}{\sigma_\ell} e^{-L_o^2/2\sigma_\ell^2} \quad \text{or} \quad w_1(\ell_h) = \sqrt{\frac{2}{\pi}} \frac{1}{\sigma_\ell} e^{-\ell_h^2/2\sigma_\ell^2}, \quad (L_o = 2\ell_h) \tag{A.1-25}$$

Using (A.1-19) with (A.1-25) in (A.1-17) gives now

$$K_h(\underline{\Delta r}) = (\gamma_o \overline{\zeta_o^2} \frac{\pi}{2}) \int_0^\infty \sqrt{\frac{2}{\pi}} \ell_h^2 e^{-\ell_h^2/2\sigma_\ell^2 - \Delta r^2/2\ell_h^2} d\ell_h/\sigma_\ell \tag{A.1-26a}$$

$$= (\gamma_o \overline{\zeta_o^2} \frac{\pi}{2}) \sqrt{\frac{2}{\pi}} \sigma_\ell^2 (\Delta r/\sigma_\ell)^{3/2} K_{3/2}(\Delta r/\sigma_\ell). \tag{A.1-26b}$$

Since ([10], p. 80)

$$K_{3/2}(x) = \sqrt{\frac{\pi}{2x}} e^{-x} [1 + \frac{1}{x}], \tag{A.1-27}$$

we note that

$$\lim_{x \to 0} \sqrt{\frac{2}{\pi}} x^{3/2} K_{3/2}(x) = 1. \tag{A.1-28}$$

Consequently, we may rewrite (A.1-26b) as

$$\left.\begin{aligned} K_h(\underline{\Delta r}) &= (\gamma_o \overline{\zeta_o^2} \frac{\pi}{2} \sigma_\ell^2) \left\{ \sqrt{\frac{2}{\pi}} (\frac{\Delta r}{\sigma_\ell})^{3/2} K_{3/2}(\Delta r/\sigma_\ell) \right\} && \text{(A.1-29a)} \\ &= \sigma_h^2 k_h(\underline{\Delta r}) = \sigma_h^2 (\frac{\Delta r}{\sigma_\ell} + 1) e^{-\Delta r/\sigma_\ell} && \text{(A.1-29b)} \end{aligned}\right\},$$

where the mean intensity is here

$$K_h(0) = \sigma_h^2 = (\gamma_o \overline{\zeta_o^2} \frac{\pi}{2} \sigma_\ell^2), \tag{A.1-30}$$

as before, cf. (A.1-20a), and the expression, { }, in (A.1-29a) is the normalized covariance, $k_h(\Delta r)$.

The associated (two-dimensional) wave number spectrum follows from (A.1-29) in (A.1-5a). Taking advantage of the surface isotropy implied by $\Delta r \to |\underline{\Delta r}| = \Delta r$ here, using (A.1-29a) we obtain*

$$W_2(\underline{k}) = \int_0^{2\pi} d\phi \int_0^{\infty} d(\Delta r)\Delta r\sigma_h^2\sqrt{\frac{2}{\pi}}\left(\frac{\Delta r}{\sigma_\ell}\right)^{3/2} K_{3/2}(\Delta r/\sigma_\ell)e^{ik\Delta r\cos\phi} \qquad (A.1\text{-}31a)$$

$$= 2\pi\sigma_h^2\sigma_\ell^2\sqrt{\frac{2}{\pi}}\int_0^{\infty} J_0(k\sigma_\ell y)K_{3/2}(y)y^{5/2}dy \qquad (A.1\text{-}31b)$$

$$W_2(\underline{k}) = \frac{6\pi\sigma_h^2\sigma_\ell^2}{[1+(k\sigma_\ell)^2]^{5/2}} = W_2(k), \qquad (k_\ell \equiv 1/\sigma_\ell), \qquad (A.1\text{-}31c)$$

$$= 6\pi\sigma_h^2 k_\ell^3/(k_\ell^2+k^2)^{5/2}, \qquad (A.1\text{-}31d)$$

again from (2), p. 410 of [10]. This spectrum, unlike that of the empirical model (A.1-7), also supports finite rms slopes, e.g., from (A.1-12),

$$\sigma^2_{h(x=y)}\big|_{\text{½ gauss}} = \frac{1}{4\pi}\int_0^{\infty} k^3 W_2(k)dk = \frac{3}{2}\left(\frac{\sigma_h^2}{\sigma_\ell^2}\right)\int_0^{\infty}\frac{x^3dx}{(1+x^2)^{5/2}} \quad (=2/3)$$

$$= \sigma_h^2/\sigma_\ell^2 \ (<\infty), \qquad (A.1\text{-}32)$$

like Case I above. Here W_2 is $O(k^{-5})$ as $k \to \infty$, while $W_{2\text{-Rayleigh}}$ is $O(k^{-6})$, and $W_{2\text{-empirical}}$ is $O(k^{-4})$. As yet, the various pdf's for ℓ_h (Cases I,II) are plausible, but not physically justified in any profound way. One task of a subsequent study will be to attempt a rational choice of $w_1(\ell_h)$, to be tested ultimately against experiment. Basically, it is the behavior as $k \to \infty$ which appears to be the controlling factor in such models.

---

*We can, of course, use (A.1-29b) directly, to obtain (A.1-31c,d).

Appendix A.2. Scattering Cross Sections: Definitions, Nomenclature, and Conditions

There is a number of variations on the concept and definitions of scattering cross section. It is therefore important to define the term explicitly, so that the different definitions can be calibrated with one another [which we shall need to do in order to effect comparisons with both the analytic results of others and the corresponding measurements (cf. [4], Secs. 2.A,b and Sec. 3 ff. for ocean wave-surface scattering)].

We begin with:

A.2-1 Incoherent Scattering Cross Sections, $\hat{\sigma}^{(0)}_{inc}$

Here we define

$$\hat{\sigma}^{(0)}_{inc} \equiv \frac{I^{(k=0)}_{incoh}\ (\text{scattering at receiver R}) \cdot R^2_{oR}}{I_{incident}(\text{at surface})\ A_{REF}} [(\text{path loss}) \times (g_T g_R)^2]^{-1}, \tag{A.2-1}$$

where I_{incoh}, $I_{incident}$ are, respectively, the intensities of the scattered and incident fields at the points indicated. The basic concept of the scattering cross section (for surfaces) is to eliminate the effects of source level and propagation, i.e., the effects of the medium--which are handled separately--when computing energy loss, and to focus on the effects of the random scattering surface itself. To keep $\hat{\sigma}^{(0)}_{inc}$ dimensionless, a reference "illumination" area, A_{REF}, is employed, whose specific form is suggested by the composite beam pattern projection on the reference or equilibrium surface $\langle\zeta\rangle \triangleq 0$: S_0. Figure A.2.1 shows the relevant geometry.

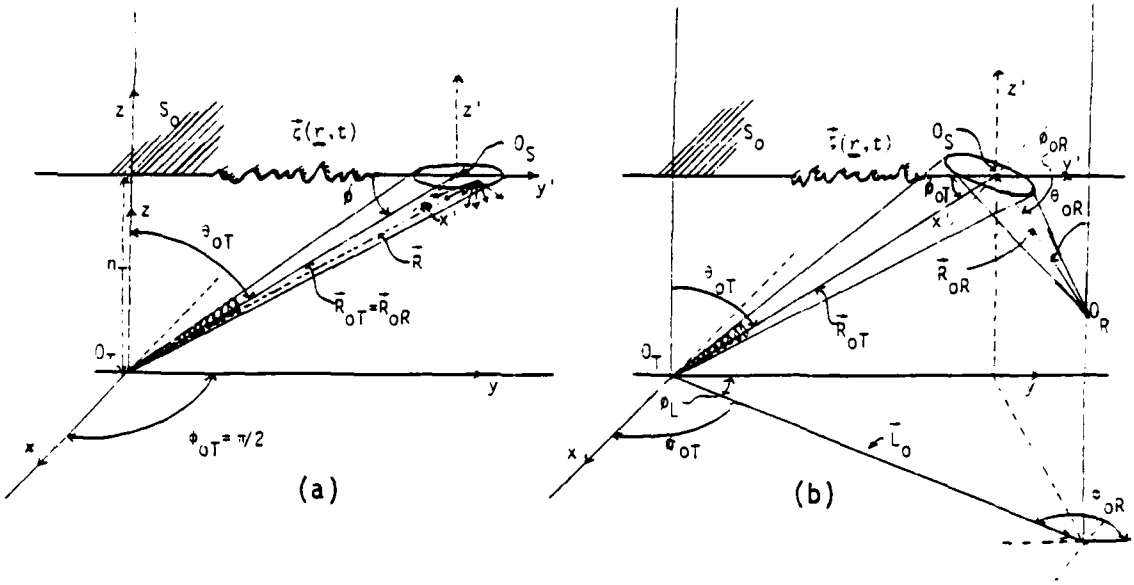

Figure A.2.1 (a) Backscatter Geometry (far-field): Monostatic scattering (R@T), vide Fig. A.2.2; (b) Bistatic Scattering (R≠T): "forward" or oblique scattering geometry, vide Fig. A.2.2.

The various factors in Eq. (A.2-1) are given by

(A.2-2a) $I_{incoh}^{(k=0)}$ (scat. at receiver) = $M_{X-\langle X\rangle}^{(0)}(0)$ = intensity of the (incoherent) scattered field at the receiver (R) [cf. Sec. 7.2 et seq.; Sec. 8 ff. of [4]];

(A.2-2b) $I_{incident}$(at surface) = $K_o(0)_{in}/(4\pi R_{oT})^2$ = intensity of the incident field at O_S, on the equilibrium scattering surface S_o;

(A.2-2c) g_T, g_R = the aperture "gain" of the transmitting and receiving systems, cf. (6.3), (6.7) of [4];

(A.2-2d) A_{REF} = a reference area on the equilibrium surface S_o, cf. Fig. A.2.1, projected by the composite T and R beam patterns. (See A.2-3 ff.);

(A.2-2e) {"path loss" (absorption) $= e^{-2a\omega_o^2 c_o T_o}$; $c_o T_o = R_{oT} + R_{oR}$; cf. Sec. 5.3, Eq. (5.18)-[4]; ω_o ($=2\pi f_o$) is the (angular) frequency of the emitted signal; $\underline{a}$ is an absorption coefficient; c_o = (mean) wave front speed of sound in the water medium;

(A.2-2f) R_{oR} = distance of the receiver (origin) from O_S, Fig. A.2.1;

(A.2-2g) R_{oT} = distance of the transmitter (origin) from O_S, Fig. A.2.1;

(A.2-2h) $\underset{\sim}{\zeta}(\underline{r},t)$ = (vector) wave surface elevation, cf. (3.5).

The definition (A.2-1) for the incoherent scattering cross section, and those similar to it ([3]-[5], [8], [9], [23]-[25], [29] in Ref. [4] here, for example) are formally independent of range (R_{oT}, R_{oR}). This is not an inherent property of the definition, however. It is a direct consequence of the far-field assumption, whereby the effective <u>coherent</u> scattering area is sufficiently small vis-à-vis source and receiver distances (R_{oT}, R_{oR}) and dimensions, cf. Sec. 5.5 and Eq. (5.31)-[4]. It also depends on the correlation distances (ℓ_x,ℓ_y) of the (components of the) random wave surface. Thus, $\hat{\sigma}^{(0)}_{inc}$ is implicitly a function of geometry, where care must be taken in its use to ensure that the conditions

governing the derivation of $I^{(k=0)}_{incoh}$ $(=M^{(0)}_{X-<X>}(0))$, (2.7a)-[4], are obeyed.*

A complete definition of the incoherent scattering cross section includes the effects of diffraction

$$\hat{\sigma}_{incoh} \equiv \hat{\sigma}^{(0)}_{incoh} + \sum_{k=1}^{\infty} \hat{\sigma}^{(k)}_{incoh} , \qquad (A.2\text{-}3)$$

where the $\hat{\sigma}^{(k)}_{incoh}$, $k \geq 1$, are formally given by (A.2-1), with $I^{(0)}_{incoh}$ replaced by the scattering intensities $I^{(k\geq 1)}_{incoh} = M^{(k)}_{X-<X>}(0)$, cf. Secs. 7.2C, 8.5 of [4].

Preliminary estimates here of the magnitude of the leading diffraction component, $\hat{\sigma}^{(1)}_{incoh}$ $(>> \hat{\sigma}^{(k\geq 2)}_{incoh})$, indicate that it is ordinarily considerably smaller than the components of the "classical" term, $\hat{\sigma}^{(0)}_{incoh}$, so that in this study we shall, at least initially, neglect the diffraction contributions.

A.2-2 Coherent Scattering Cross Sections, $\hat{\sigma}^{(0)}_{coh}$

The coherent scattering cross section, $\hat{\sigma}^{(0)}_{coh}$, is formally the same as $\hat{\sigma}^{(0)}_{incoh}$, (A.2-1), except that now the incident intensity (A.2-2b) becomes

$$I_{incident}(\text{at the receiver})_{coh} = K_o(0)_{in}/\{4\pi(R_{oT} + R_{oR})\}^2 \qquad (A.2\text{-}4)$$

which is the "mirror reflection" term. Thus, $I_{incid\text{-}coh} = (1/4)I_{incid\text{-}incoh}$, cf. (A.2-2b). In addition, $I^{(k=0)}_{incoh}$ is replaced by the coherent component $M^{(0)}_{<X>}(0)$, cf. Sec. 7.2B, Eq. (8.7), [4]. Since only the "classical" or (k=0) component of the scattered field, contains a

---

*The factors 4π in (A.2.2a,b), and in (2.9), (2.10b(ff., etc., arise because of our definition of the green's function, (5.8)-[4], and source function (5.3a)-[4] in the equations of propagation (here a Helmholtz medium). Thus, our acoustic field is $\alpha_M = \alpha/4\pi$, where α is derived from a green's function source of the form $-4\pi\delta(\underline{R}-\underline{R}')\delta(t-t')$. However, because of the particular form of the definition of $\hat{\sigma}^{(0)}$ used here and generally, the scaling of the field is immaterial, as is required in any useful definition.

potentially coherent contribution (excluding any direct field which may be received under certain mutual geometries), the complete coherent scatter cross section is now specifically

$$\hat{\sigma}^{(0)}_{coh} \equiv \frac{I^{(0)}_{coh}(\text{scattering at R})\, R^2_{oR}}{I_{incid}(\text{at the receiver R})\, A_{REF}} \{\text{path loss} \times (g_T g_R)^2\}^{-1}, \quad \text{(A.2-5a)}$$

or

$$\hat{\sigma}^{(0)}_{coh} = \frac{R^2_{oR}\{4\pi(R_{oR} + R_{oT})\}^2\, M^{(0)}_{<X>}(0)}{(g_T g_R)^2\, A_{REF}\, K_o(0)_{in} \cdot (\text{path loss})} \cdot \quad \text{(A-2.5b)}$$

A.2-3 The Reference Area, A_{REF}

The reference area, A_{REF}, appearing in the above definitions of the scattering cross sections, (A.2-1); (A.2-5), while arbitrary, is dependent on the beam pattern projections on S_o. From Section 6.5 IV, (6.56) of [4], our choice of reference area is specifically

$$A_{REF} = A_1/2, \quad A_1 = 2\pi/\sqrt{AB(\theta_{oT})}, \quad \text{(A.2-6)}$$

where A_1 is the projected area (on S_o), here specifically of the combined gaussian-omni-directional beam patterns used in this study and in [4]; $AB(\theta_{oT})$ are parameters of the projected beam pattern on S_o, cf. 6.3; also Secs. 6.4, 6.5 of [4] for details.

A.2-4 General Geometry in Detail: The Received Scattered Wave

For the detailed development of the analysis it is now necessary to describe the general geometry of the underice surface in relation to the source and receiver in our current "one-bounce" model. This geometry of the general (far-field) source-surface-receiver configuration is shown in Fig. A.2-2, in more detail (cf. Fig. A.2-1).

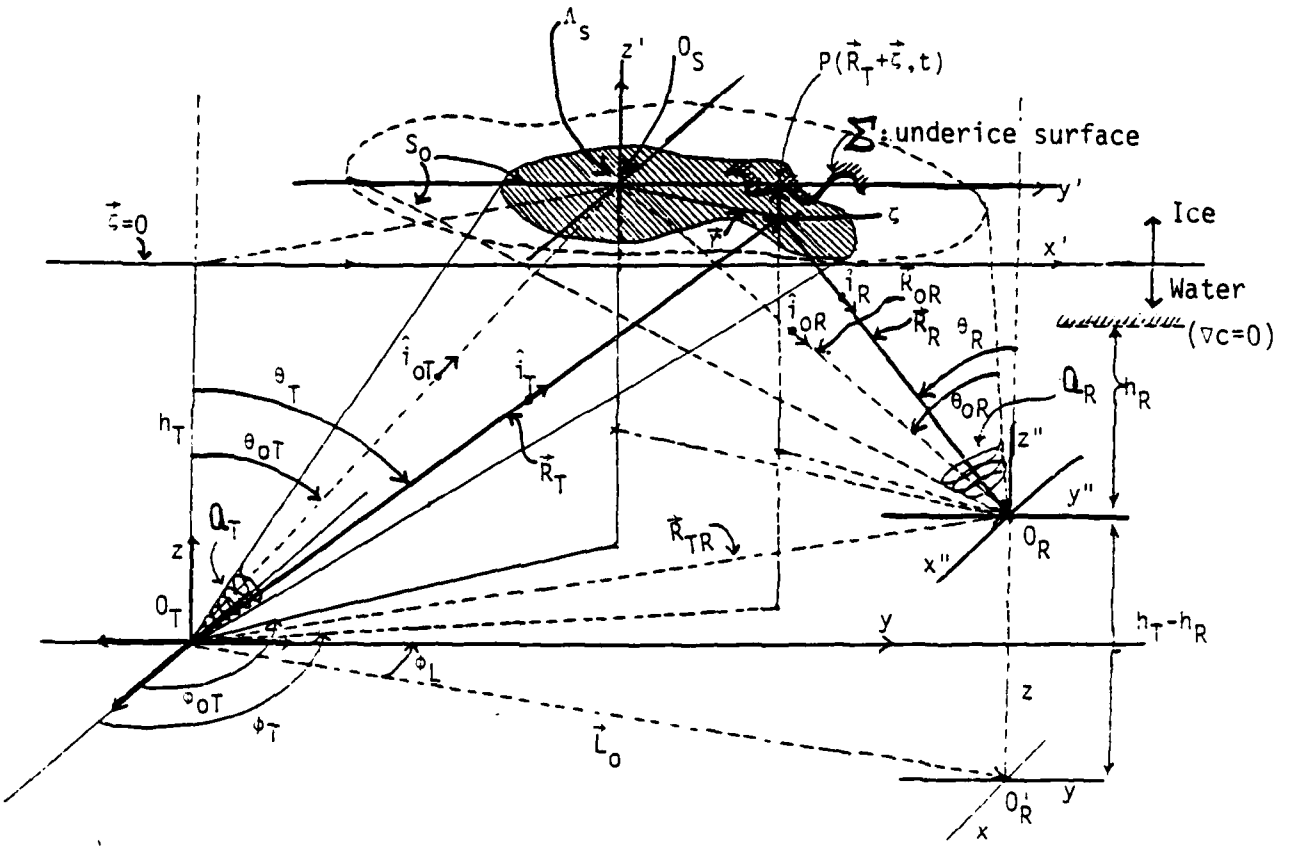

Figure A.2-2 Geometry of the transmitter (@ O_T), underice surface (Σ), receiver (at O_R), showing surface elevation $\vec{\zeta}$ above $\vec{\zeta} = 0$: S_o, and the common region of illumination (shaded), on S_o due to overlapping beam patterns $\mathcal{Q}_T$, $\mathcal{Q}_R$; (here $\nabla c = 0$).

The associated received scattered wave (exclusive of diffraction terms) is (from (7.7-[4])

$$\left. x^{(0)}(t) \right|_{\substack{\text{far-field} \\ \text{narrow-band}}} = A_o \int_{Br1} S_{in}(s/2\pi i) F_S^{(0)}(s|\zeta(\underline{r},t)\ldots|f_o) e^{st} \frac{ds}{2\pi i} , \tag{A.2-7}$$

where the Total Surface Spreading Function (TSSF) is now specifically

$$F_S^{(0)} \triangleq \frac{e^{-a\omega_o^2 c_o T_o}}{(4\pi)^2 R_{oT} R_{oR}} \int_{S_o} \frac{s}{c_o} R_o S\left[\frac{\hat{n}\cdot(\hat{i}_{oT}-\hat{i}_{oR})}{n_z}\right] Q_{RT} \cdot e^{-(s/c_o)[(\underline{r}+\underline{\zeta})\cdot 2\underline{\alpha}_o + c_o T_o]}\, dxdy, \tag{A.2-7a}$$

cf. (7.7)-[4], subject to the conditions of Sec. 5.5, [4], summarized here in A.2-15 following.

The various elements of (A.2-7) are described below. These are:

A_S = effective "illuminated" surface area, by joint beam projection in S_o, cf. Sec. 6.3, Fig. 6.1, [4]. (A.2-8)

$dS_o = \underline{dr} = dx'dy' = dxdy$ on S_o: $\vec{\zeta} = 0$; with $d\Sigma = dS_o/n_z$; (A.2-8a)

$\boxed{\underline{r}' = \underline{r} + \underline{\zeta}}$, where $\underline{r}'$ is always on the underice surface ; (A.2-8b)

$\underline{r} = \hat{i}_x x + \hat{i}_y y$; [(x',y')-system is simply a translation of the (x,y)-system] (A.2-8c)

$T_o = (R_{oT} + R_{oR})/c_o$: time-delay from $O_T \to O_S \to O_R$: (A.2-8d)

$\hat{i}_{oT}, \hat{i}_{oR} \equiv \underline{R}_{oT,oR}/|\underline{R}_{oT}, \underline{R}_{oR}|$: unit vectors; (A.2-8e)

$\hat{i}_T, \hat{i}_R \equiv \underline{R}_{T,R}/|\underline{R}_{T,R}|$: unit vectors, to projection of scattering point on Σ upon S_o; (A.2-8f)

$R_T, R_R, R_{OT}, \ldots = |\underline{R}_T|, |\underline{R}_R|$, etc., distances; (A.2-8g)

$t' = t - \Delta t_{dS}$ = doppler-shifted epoch; $(\underline{r}', t')$ are on the underice surface Σ; (A.2-8h)

$\Delta t_{dS} = \hat{i}_T \cdot \underline{r}'(\underline{r},t) = \hat{i}_T \cdot \{\underline{r} + \underline{\zeta}(\underline{r}, t - R_R/c_o)\}$: $R_R \doteq R_{oR} - \hat{i}_{oR}\cdot\underline{r}$; (A.2-8i)

$\boxed{\underline{\zeta}(\underline{r},t)}$ = (vector) elevation of the ice-bottom surface, vs. $\underline{\zeta} = 0$, the plane S_o; cf. Figs. 2.2. (A.2-8j)

$a = \tau_o/2c_o$ = absorption coefficient ($\sec^{-2}$/meter), cf. (5.18)-[4]. (A.2-8k)

Also, we have

Q_{RT} = (complex) beam pattern of R,T; A_o = injected signal amplitude. (A.2-8l)

In addition, we write

$n_z = (1 + \zeta_x^2 + \zeta_y^2)^{-\frac{1}{2}}$; $\zeta_x, \zeta_y = \frac{\partial \zeta}{\partial x}, \frac{\partial \zeta}{\partial y}$: surface slopes (A.2-9a)

$\underset{\sim}{\hat{n}}$ = normal to surface Σ, $(\underset{\sim}{\hat{i}}_x \zeta_x + \underset{\sim}{\hat{i}}_y \zeta_y - \underset{\sim}{\hat{i}}_z) n_z$; (inward normal = $-\underset{\sim}{\hat{i}}_z$) (A.2-9b)

$\underset{\sim}{\nu}_{oT}, \underset{\sim}{\nu}_{oR} = \underset{\sim}{\hat{i}}_{T,R} f_o / c_o$ = beam-steering wave numbers, cf. (5.13b), (5.7a), [4]; (A.2-9c)

$\underset{\sim}{R}_{TR} = \vec{L}_o + \underset{\sim}{\hat{i}}_z (h_T - h_R)$, cf. Fig. A.2-2; vector distance between O_T and O_R. (A.2-9d)

From Fig. A.2-2, it is readily shown that the unit vectors $\underset{\sim}{\hat{i}}_T$, $\underset{\sim}{\hat{i}}_R$ become for these bistatic configurations

$$\underset{\sim}{\hat{i}}_T \Big|_{S_o} = \underset{\sim}{R}_T / |\underset{\sim}{R}_T| = \underset{\sim}{\hat{i}}_x \cos\phi_T \sin\theta_T + \underset{\sim}{\hat{i}}_y \sin\phi_T \sin\theta_T + \underset{\sim}{\hat{i}}_z \cos\theta \qquad \text{(A.2-10a)}$$

$$\underset{\sim}{\hat{i}}_R \Big|_{S_o} = R_R / |\underset{\sim}{R}_R| = -\{\underset{\sim}{\hat{i}}_x R_T \cos\phi_T \sin\theta_T + \underset{\sim}{\hat{i}}_y (R_T \sin\phi_T \sin\theta_T - L_o) + \underset{\sim}{\hat{i}}_z h_R\} / R_R \,, \qquad \text{(A.2-10b)}$$

where

$$R_R = (R_T^2 \sin^2\theta_T + L_o^2 - 2R_T L_o \sin\phi_T \sin\theta_T + h_R^2)^{\frac{1}{2}}, \text{ and} \qquad \text{(A.2-10c)}$$

$$\boxed{\phi_{(o)T} = \phi_{(o)R} - \pi/2.}$$

[For $\underset{\sim}{\hat{i}}_{oT}$, $\underset{\sim}{\hat{i}}_{oR}$ we simply replace R_T by R_{oT}, $\phi_T \to \phi_{oT}$, etc. in (A.2-10).] We also find it convenient to write

$$\boxed{2\underset{\sim}{\alpha}_{(o)} \equiv \underset{\sim}{\hat{i}}_{(o)T} - \underset{\sim}{\hat{i}}_{(o)R}} = \underset{\sim}{\hat{i}}_x (1 + R_{(o)T}/R_{(o)R} \cos\phi_{(o)T} \sin\theta_{(o)T}$$

$$+ \underset{\sim}{\hat{i}}_y \{(1 + R_{(o)T}/R_{(o)R}) \sin\phi_{(o)T} \sin\theta_{(o)T} - L_o/R_{(o)R}\}$$

$$+ \underset{\sim}{\hat{i}}_z (\cos\theta_{(o)T} + \cos\theta_{(o)R}), \qquad \text{(A.2-11)}$$

cf. the exponent in (A.2-7a). [Again, for the reference vectors $\underset{\sim}{\hat{i}}_{oT}$, $\underset{\sim}{\hat{i}}_{oR}$, $\underset{\sim}{R}_{oT}$, etc., we set $R_T \to R_{oT}$, $\phi_T \to \phi_{oT}$, etc., to get $2\underset{\sim}{\alpha}_o \equiv \underset{\sim}{\hat{i}}_{oT} - \underset{\sim}{\hat{i}}_{oR}$, as indicated in (A.2-11).]

A critically important simplification of our canonical result (A.2-7) results from the ability to employ "narrow beams" (N.B.), e.g., beams narrow enough so that the mutually "illuminated" surface Σ (= S_o) (i.e., the shaded region in Fig. A.2-2, for example) is sufficiently small that the spatial geometry (~R_T, R_R, etc.) for source and receiver change little over the "illuminated" surface region (~ S_o). Thus, we can replace $\underline{R}_T$ by $\underline{R}_{oT}$, θ_T by θ_{oT}, etc., and most important, note that the angle-dependent quantities in $F_S^{(0)}$, (A.2-7a) can also be replaced by the (constant) reference quantities θ_{oT}, ϕ_{oT}, etc. This results in a "factoring" of the beam patterns, in that they now will depend only on their projections on the surface about O_S, and not on the coördinates of the w surface away from O_S. [For details, see Section 6, [4].]

A.2-5 Parameters of Eq. (3.6): $\hat{\sigma}_{inc}^{(0)}$, $R_\zeta >> 1$

The various elements of (3.6) are specifically:

(A.2-12)

- $\overline{R_o^2}$, $\overline{R_o}$ = mean-square, mean, reflection coefficients (=1, for water/air and water/ice interfaces);
- $\overline{S^2}$, $\overline{S}$ = mean-square, mean, shadowing function, see Sec. 7.4C-[4], and
- σ_{Lx}^2, σ_{Ly}^2 = $\langle \zeta_{Lx}^2 \rangle$, $\langle \zeta_{Ly}^2 \rangle$: ($\zeta_{Lx} = \frac{\partial \zeta_L}{\partial x}$, etc.): mean-square slopes of the "low-frequency" ice surface component, cf. Sec. 7.4B-[4], and
- σ_H^2 = $\langle \zeta_H^2 \rangle$: mean-square height (about $\langle \zeta_H \rangle = 0$) of the high-frequency ice surface component;
- W_H = surface wave number intensity spectrum of ζ_H (cf. (3.5) and Appendix (A.1)) with

$$\sigma_G^2 \rho_c(\underline{\Delta r}, 0) = \int_{\underline{k}_D}^{\infty} W_c(\underline{k}|0) \cos(\underline{k} \cdot \underline{\Delta r}) \frac{d\underline{k}}{2\pi^2} ,$$

- A_1 = Eq. (A.2-6);
- b_o = $\cos \theta_{oT} + \cos \theta_{oR}$.

The directional vector $2\underline{\alpha}_o$ is given by (A.2-11): $\underline{\alpha}\to\underline{\alpha}_o$, for arbitrary angles of illumination and observation.

Important special cases of (A.2-11) are:

(i). Backscatter (R@T): ($L_o = 0$; $\theta_{oR} = \theta_{oT}$; $\hat{\underline{i}}_{oR} = -\hat{\underline{i}}_{oT}$; $R_{oR} = R_{oT}$; $h_R = h_T$; $\phi_{oR} = \phi_{oT} + \pi/2$; cf. Fig. 2.2).

$$\therefore 2\underline{\alpha}_o = 2(\hat{\underline{i}}_x \cos\phi_{oT} \sin\theta_{oT} + \hat{\underline{i}}_y \sin\phi_{oT} \sin\theta_{oT} + \hat{\underline{i}}_z \cos\theta_{oT}); \tag{A.2-13a}$$

$$(\alpha_{ox}^2 + \alpha_{oy}^2 + \alpha_{oz}^2)/\alpha_{oz}/2 = 2/\cos\theta_{oT}. \tag{A.2-13b}$$

(ii). Bistatic at the Snell Angle ($R \neq T$): $L_o \neq 0$

$$\left.\begin{aligned} &(\hat{\underline{i}}_{oR})_x = (\hat{\underline{i}}_{oT})_x \quad \text{when } \phi_{oT} = \pi/2 = (\phi_{oR} - \pi/2);\\ &(\hat{\underline{i}}_{oR})_y = (\hat{\underline{i}}_{oT})_y \quad \text{when } L_o = (R_{oT} + R_{oR})\sin\theta_{oT};\\ &(\hat{\underline{i}}_{oR})_z = -(\hat{\underline{i}}_{oT})_z \quad \text{when } \theta_{oR} = \theta_{oT}. \end{aligned}\right\} \text{Snell plane} \tag{A.2-14a}$$

$$\therefore 2\underline{\alpha}_o = 2\hat{\underline{i}}_z \cos\theta_{oT}, \text{ or } \underline{\alpha}_o = \hat{\underline{i}}_z \cos\theta_{oT}; \tag{A.2-14b}$$

$$(\alpha_{ox}^2 + \alpha_{oy}^2 + \alpha_{oz}^2)/\alpha_{oz}/2 = 2\cos\theta_{oT}. \tag{A.2-14c}$$

Otherwise, (A.2.11) is the general relation.

The principal assumptions and approximations pertaining to our general high-frequency results (3.6), (3.7), are:

(A.2-15)
(1). Far-field (Fraunhofer) geometries, cf. Sec. 5.5 of [4], with $\nabla c = 0$;
(2). Narrow-band signals (so that we may treat time parametrically in the moving wave (or ice) surface vis-à-vis the acoustic signal); cf. remarks after Eq. (5.21b)-[4];
(3). Narrow beams (cf. Sec. 6.6-[4]; at least one narrow-beam;
(4). Neglects diffraction terms: k=1: "Diffuse" scatter; $k \geq 2$: multiple scatter (cf. Sec. 3.3; also Sec. 8.5, of [4]);

(5). Small Rayleigh numbers for the small-scale surface, ζ_H: $R_H \equiv (k_o b_o \sigma_H)^2 << 1$;

(6). The surface (ζ_H) is "small-scale," e.g., $\ell_H << \ell_L$: the correlation distance of the low wave-number component is much larger than that of the high wave-number contribution;

(A.2-15) (7). The small-scale surface is statistically independent of the ζ_H-surface component (vide remarks in Sec. 7.3A, Eq. (7.19) et seq., [4]);

(8). Both components of the wave surface are essentially homogeneous and stationary, at least over the "illuminated" area and for times long compared to the duration of the incident signal (in the case of platform motion).

Appendix A.3: Second-Order Probability Densities of the Mixed or Gauss-Composite K,S Process, Eq. (2.1)

Our task here is to see if it is possible to generalize the mixed K,S process, described in Eq. (2.1) by the weighted sum of two first-order gaussian pdf's, by a suitably weighted second-order pdf, consisting of a weighted sum of second-order gaussian processes.

We begin with (2.1) et seq., which we rewrite here for the empirical fit to the Lyon data for the underwater ice elevation ζ, as the first-order pdf

$$w_1(\zeta) = \frac{b_1}{\sqrt{2\pi\sigma_S^2}} e^{-(\zeta-m_S)^2/2\sigma_S^2} + \frac{b_2}{\sqrt{2\pi\sigma_K^2}} e^{-(\zeta-m_K)^2/2\sigma_K^2}, \qquad \text{(A.3-1)}$$

for which specifically

$$\left.\begin{aligned} &b_1 = 0.93\underline{0}; \quad b_2 = 1-b_1 = 0.07\underline{0}; \quad (b_1+b_2 = 1) \\ &m_S = 4.5\underline{0}(m); \; m_K = 12.5(m) \\ &\sigma_S = 1.0\underline{0}(m); \; \sigma_K = 3.0\underline{0}(m) \end{aligned}\right\} \qquad \text{(A.3-1a)}$$

The associated characteristic function (c.f.) (2.4), or (A.3-1) is therefore

$$F_1(i\xi) = b_1 e^{im_S\xi-\sigma_S^2\xi^2/2} + b_2 e^{im_K\xi-\sigma_K^2\xi^2/2} \qquad \text{(A.3-2)}$$

$$= b_1 F_{1S}^{(1)} + b_2 F_{1K}^{(1)}. \qquad \text{(A.3-2a)}$$

Accordingly, we obtain

$$\overline{\zeta} = -i \left.\frac{dF_1^{(1)}}{d\xi}\right|_{\xi=0} = b_1 m_S + b_2 m_K = 5.1 \text{ (m)}; \qquad \text{(A.3-4a)}$$

$$\overline{\zeta^2} = -\left.\frac{d^2F_1}{d\xi^2}\right|_{\xi=0} = b_1(\sigma_S^2 + m_S^2) + b_2(\sigma_K^2 + m_K^2) = 31.3 \text{ (m}^2\text{)}; \qquad \text{(A.3-4b)}$$

$$\therefore \sigma_\zeta^2 \equiv \overline{\zeta^2} - \bar{\zeta}^2 \equiv \text{var}\,\zeta = b_1\sigma_S^2 + b_2\sigma_K^2 + b_1 b_2 (m_S - m_K)^2 = (2.38)^2\ (m^2), \tag{A.3-4c}$$

since $b_{1,2} = 1 - b_{2,1}$, cf. (A.3-1a).

In our effort to construct a second-order pdf, $w_2(\zeta_1,t_1;\zeta_2,t_2)$, which is a valid generalization of the first-order pdf (A.3-1), we must require that the following conditions be obeyed:

I. The first and second moments derived from w_2 (or the associated c.f., $F_{2\text{-}\zeta}$) are the same as those obtained from the first-order w_1, (A.3-1), viz., (A.3-4a,b), with the same variance (A.3-4c), e.g., var ζ_1 = var ζ_2 = var ζ, for ζ now postulated to be <u>homogeneous</u>. [If this latter condition is removed, then the <u>form</u> of var $\zeta_{1,2}$ is to be the same as that of var ζ.]

II. When $\underset{\sim}{\Delta r} = \underset{\sim}{r}_2 - \underset{\sim}{r}_1$ (in the (x,y)-plane of $\zeta(\underset{\sim}{r})$) becomes infinite, i.e., $\underset{\sim}{\Delta r} \to \pm\infty$, then

$$\lim_{\Delta r \to \pm\infty} F_{2\text{-}\zeta} = F^{(1)}_{1\text{-}\zeta} F^{(2)}_{1\text{-}\zeta} = F_1(i\xi_1)_\zeta F_1(i\xi_2)_\zeta: \tag{A.3-5}$$

ζ_1, ζ_2 are (second-order) independent as $\Delta r \to \pm\infty$, <u>where $F_1(i\xi)_\zeta$ is given by (A.3-2)</u>!

Condition II then requires that the second-order c.f. $F_{2\text{-}\zeta}$ have the form

$$\boxed{F_{2\text{-}\zeta} = b_1^2 F_{2S} + b_1 b_2 F^{(1)}_{1S} F^{(2)}_{1K} + b_1 b_2 F^{(1)}_{1K} F^{(2)}_{1S} + b_2^2 F_{2K},} \tag{A.3-6}$$

where $F_{1S,K}$ has the <u>form</u> (A.3-2a), for inasmuch as $\lim_{\underset{\sim}{\Delta r}\to\pm\infty} F_{2S,2K} = F^{(1)}_{1S,1K} F^{(1)}_{1S,1K}$, we see that

$$\lim_{\underset{\sim}{\Delta r}\to\pm\infty} F_{2\text{-}\zeta} = (b_1 F^{(1)}_{1S} + b_2 F^{(1)}_{1K})(b_1 F^{(2)}_{1S} + b_2 F^{(2)}_{2K}) = F^{(1)}_{1\text{-}\zeta} F^{(2)}_{1\text{-}\zeta}\ , \tag{A.3-7}$$

with $F^{(1)}_{1\text{-}\zeta}$, etc., given formally by (A.3-2a). Note that no specific statistical structure for (ζ_S,ζ_K,ζ) has yet been imposed. [Also note that $F_{2\text{-}\zeta|\xi_1=\xi_2=0} = (b_1^2 + 2b_1b_2 + b_2^2) = (b_1 + b_2)^2 = 1$, all $\underset{\sim}{\Delta r}$, as required.]

Now, let us require that $F^{(1)}_{1-\zeta}$ be given specifically by the gaussian first-order composite form (A.3-2) and that ζ_S, ζ_K and ζ, are homogeneous processes. Then the (first-order) first- and second moments are given by (A.3-4), as required. However, according to (A.3-7) this has been established only for $F_{2-\zeta}$ in the limit $\Delta r \to \pm\infty$. We need now to determine whether I (and II) are satisfied in the general case $0 \leq |\underline{\Delta r}| < \pm\infty$. Accordingly, for $F_{2-\zeta}$ to reduce to the gaussian form (A.3-2) we require that ζ_K, ζ_S be second-order gaussian processes, so that (A.3-6) becomes explicitly (for these homogeneous cases)

$$F_{2-\zeta} = b_1^2 e^{im_S\xi_1+im_S\xi_2-\sigma_S^2(\xi_1^2+\xi_2^2+2\rho_S\xi_1\xi_2)}$$

$$+ b_1b_2 e^{im_S\xi_1+im_K\xi_2-\frac{1}{2}[\sigma_S^2\xi_1^2+\sigma_K^2\xi_2^2+\sigma_S\sigma_K\rho_{SK}\xi_1\xi_2+\sigma_S\sigma_K\rho_{KS}\xi_1\xi_2]}$$

$$+ b_1b_2 e^{im_K\xi_1+im_S\xi_2-\frac{1}{2}[\sigma_K^2\xi_1^2+\sigma_S^2\xi_2^2+\sigma_S\sigma_K\rho_{KS}\xi_1\xi_2+\sigma_S\sigma_K\rho_{SK}\xi_1\xi_2]}$$

$$+ b_2^2 e^{im_K\xi_1+im_K\xi_2-\frac{1}{2}\sigma_K^2(\xi_1^2+\xi_2^2+2\rho_K\xi_1\xi_2)}. \qquad \text{(A.3-8)}$$

Clearly, since $\lim_{\underline{\Delta r}\to\pm\infty} \rho_S, \rho_{KS}, \rho_{SK} \to 0$, (A.3-8) reduces directly to the form (A.3-7), as required by II, (A.3-5). Moreover, $-1 \leq \rho_S, \rho_{KS}, \rho_{SK} \leq 1$: these normalized auto- and cross-covariances are, by definition, bounded as indicated. In addition, the quadratic forms in the various exponents of (A.3-8) must be at least positive semi-definite. This means that no adjustable scale factors can be introduced as coefficients of ρ_S, ρ_{KS}, etc., or of σ_S^2, σ_K^2, etc.

Next, let us obtain the various second-order moments associated with (A.3-8). Inasmuch as $F_{2-\zeta}$ here reduces to (A.3-7), with $F^{(1)}_{1-\zeta}$, etc., given by (A.3-2), $\zeta_1^2 = \zeta_2^2 = \zeta^2$, (A.3-4b), in these homogeneous cases. For the covariance $K_\zeta(\underline{\Delta r})$ we get directly on differentiation of (A.3-8),

$$K_\zeta(\underline{\Delta r}) \equiv \overline{\zeta_1\zeta_2} - \bar{\zeta}_1\bar{\zeta}_2 = -\frac{\partial^2}{\partial\xi_1\partial\xi_2} F_{2-\zeta}\Big|_{\xi_1=\xi_2=0} - (b_1m_S+b_2m_K)^2 \qquad \text{(A.3-9a)}$$

$$= b_1^2\sigma_S^2\rho_S + b_2^2\sigma_K^2\rho_K + b_1b_2\sigma_S\sigma_K(\rho_{SK}+\rho_{KS}), \qquad \text{(A.3-9b)}$$

which vanishes, as required, when $\underset{\sim}{\Delta r} \to \pm\infty$, since $\lim_{\underset{\sim}{\Delta r}\to\pm\infty} \rho_S$, (etc.) $\to 0$. We can rewrite (A.3-9b), using $b_1 = 1-b_2$, etc., as

$$K_\zeta(\underset{\sim}{\Delta r}) = b_1\sigma_S^2\rho_S + b_2\sigma_K^2\rho_K + b_1b_2\{\sigma_S\sigma_K(\rho_{SK}+\rho_{KS}) - \sigma_S^2 - \sigma_K^2\}. \qquad \text{(A.3-10)}$$

The behavior as $\underset{\sim}{\Delta r} \to 0$ now needs to be examined. We have for (A.3-10)

$$K_\zeta(0) = b_1\sigma_S^2 + b_2\sigma_K^2 + b_1b_2(2\sigma_S\sigma_K\rho_o - \sigma_S^2 - \sigma_K^2) = \overline{\zeta^2} - \bar{\zeta}^2; \qquad \text{(A.3-11)}$$

$$\rho_o \equiv \rho_{SK}^{(0)} = \rho_{KS}^{(0)}.$$

This is to be compared with $\overline{\zeta^2}$ calculated directly from the first-order c.f. (A.3-2), viz. (A.3-4c):

$$(\text{var } \zeta = \overline{\zeta^2} - \bar{\zeta}^2)_{\text{1st-order}} = b_1\sigma_S^2 + b_2\sigma_K^2 + b_1b_2(m_S-m_K)^2. \qquad \text{(A.3-12)}$$

We see at once that it is quite impossible for (A.3-11) and (A.3-12) to be equal ($b_1 \neq b_2 \neq 1.0$) unless $m_S = m_K$ <u>and</u> $\rho_{SK}^{(0)} = \rho_{KS}^{(0)} = +1$, with $\sigma_K = \sigma_S$: then the two (K,S) processes are second-moment identical, and correlated. This is not at all physically likely, so we must discard it as an acceptable model.

We note that changing the weighting, b_1b_2 (in such a way as to obey II, cf. (A.3-7)), does not help us achieve agreement between var ζ_{1st} (A.3-12) and $K_\zeta(0)$, (A.3-11). For example, let us replace b_1b_2 by $b_1b_2(1-\rho_{SK})$, $b_1b_2(1-\rho_{KS})$ respectively in (A.3-8). This gives the correct form for $\underset{\sim}{\Delta r} \to \pm\infty$, (A.3-7), but merely inserts a factor $1-\rho_{SK}$, $1-\rho_{KS}$ with ρ_{SK}, ρ_{KS} in (A.3-10), (A.3-11), which again does not allow an equality between (A.3-11) and (A.3-12), except in the trivial case noted above.

However, if we set $b_1=1$ ($\therefore b_2=0$), or vice versa, we do get agreement, as we would expect, since only one gauss component is present. Of course, the choice $b_1=1$ ($b_2=0$) gives a good fit to the first-order data except for the important tails (represented by the K-gauss process here). In retaining this model (Model I), we make the comparison indicated in Sec. 2.1, Eq. 2.7: we choose here a single gauss process, ζ, whose mean and variance are those of the <u>gauss composite</u> process obeying (2.1), or (A.3-1)-(A.3-4) above. Thus our Models Ia,b are taken to be a single process, with first-order, first- and second-moments determined from the Lyon data fit (2.1).

Before we note the implication of the above, we observe that using a composite gauss process

$$\zeta_{comp} = a_1\zeta_S + a_2\zeta_K, \qquad (0 \leq a_1, a_2 \leq 1), \tag{A.3-13}$$

rather than the gauss composite process (described by (A.3-1), (A.3-2)), also does not permit an equivalence between the two (unless $a_2 = 0$, for example). This is easily seen, for

$$\bar{\zeta}_{comp} = a_1\bar{\zeta}_S + a_2\bar{\zeta}_K, \quad \therefore a_1 = b_1, \quad \bar{\zeta}_S = m_S; \quad a_2 = b_2; \quad \bar{\zeta}_K = m_K$$

$$(0 \leq b_1, b_2 \leq 1) \tag{A.3-14}$$

Similarly, we get directly

$$\text{var}\,\zeta_{comp} = b_1^2\sigma_S^2 + b_2^2\sigma_K^2 + b_1b_2\{2K_{SK}(0) - \sigma_S^2 - \sigma_K^2\}; \tag{A.3-15}$$

$$K_{SK}(0) = M_{SK}(0) - m_Sm_K; \quad M_{SK}(0) = \overline{\zeta_S\zeta_K}. \tag{A.3-15a}$$

From (A.3-4c) and (A.3-15), we can write

$$\text{var}\,\zeta_{comp} = \sigma_\zeta^2 - b_1b_2\{\sigma_K^2 + \sigma_S^2 - 2\sigma_S\sigma_K\rho_{KS}(0) + (m_S-m_K)^2\} > 0, \tag{A.3-16}$$

with $\rho_{KS}(0) = \rho_{SK}(0) = K_{SK}(0)/\sigma_S\sigma_K$. Consequently,

$$\text{var}\,\zeta_{comp} > \sigma^2 > b_1b_2\{\sigma_K^2 + \sigma_S^2 - 2\sigma_S\sigma_K\rho_{KS}(0) + (m_S-m_K)^2\} > 0, \tag{A.3-17}$$

so that $\text{var}\,\zeta_{comp} > \sigma_\zeta^2$ (> 0) always: these two first-order processes (composite gauss, (A.3-13), and gauss composite (2.1)) are not the same. We need proceed no further in the second-order cases: the second-order forms cannot reduce to a common first-order, (2.1).

In summary, our principal results here and their implications are concisely:

I. It is not possible to construct a second-order gauss composite process which reduces to the prescribed first-order process [(2.1)], having the same second-order (and therefore, higher-order) moments.

II. It is possible to construct a single-component process with the same first- and second- (first-order) moments. This is the procedure followed in the substance of this Report, for which Model I is thus essentially treated as a single-component process, cf. (2.16) ff., and (2.7) et seq. The moments used explicitly are obtained by a combination of fitting to the data and physical-model building.

References

[1]. W. K. Lyon, "Ocean and Sea Ice Research in the Arctic Ocean via Submarine," Trans. N.Y. Acad. of Sciences 23, 662-674, 1961.

[2]. R. H. Mellen, "Underwater Acoustic Scattering from Arctic Ice," J. Acous. Soc. Amer. 40, 1200-1201, 1966. See, also, [24] ff.

[3]. D. A. Rothrock and A. S. Thorndike, "Geometric Properties of the Underside of Sea Ice," J. of Geophys. Research 85, No. C7, pp. 3955-3963, July, 1980.

[4]. D. Middleton, "Acoustic Scattering Cross-Sections for Truly Composite Wind-Wave Surfaces: Scattering Without Bubbles," NUSC Tech. Document No. 7205, Aug. 20, 1984, NUSC, New London, Conn. 06320.

[5]. R. H. Mellen, F. R. DiNapoli, and R. L. Deavenport, "Underwater Acoustics in the Arctic Ocean," paper in Proceedings of NATO Advanced Study Institute on "Adaptive Methods in Underwater Acoustics," July 30-Aug. 10, 1984, Lüneburg, Germany; to be published, by D. Reidel, Dordrecht, Holland, Spring, 1985. See, also, [24] ff.

[6]. D. Middleton, An Introduction to Statistical Communication Theory, McGraw-Hill (New York), 1960; Chapter 7.

[7]. P. L. Stocklin, Memorandum to Drs. R. H. Mellen (B.K. Dynamics, Inc., New London, Conn.) and F. R. DiNapoli (NUSC, New London, Conn.), "Preliminary Statistical Analysis of Underice Profile," April 9, 1984 (courtesy of R. H. Mellen to D. Middleton).

[8]. D. Middleton, Ref. [4], Secs. 2.1; Sec. 3.2; and discussion in Sec. 4; also, Sec. 7.3 et seq.

[9]. _____, "Doppler Effects for Randomly Moving Scatterers and Platforms," JASA 61, No. 5, May, 1977, pp. 1231-1250.

[10]. G. N. Watson, Theory of Bessel Functions, McMillan (New York), 1944.

[11]. L. Brekhovskikh and Yu. Lysanov, Fundamentals of Ocean Acoustics, Springer Series in Electrophysics Vol. 8, 1982, Springer-Verlag, New York (N.Y.).

[12]. F. G. Bass and I. M. Fuks, Wave Scattering from Statistically Rough Surfaces, Transl. & Ed. by C. B. Vesecky and J. F. Vesecky, International Series in Natural Philosophy, Vol. 93, 1979, Pergamon Press, New York.

[13]. E. Bahar, D. E. Barrick, and M. A. Fitzwalter, "Computations of Scattering Cross-Sections for Composite Surfaces and the Specification where Spectral Splitting Occurs," IEEE Trans. on Antennas and Propagation, Vol. AP-31, No. 5, Sept. 1983, pp. 698-709. [See also Refs. [22]-[24], [30], [31], [44] of Ref. [4] above.

[14]. E. Bahar, "Scattering Cross Sections for Composite Random Surfaces--Full Wave Analysis," Radio Science, Vol. 16, No. 6, Nov.-Dec., 1981, pp. 1327-1335.

[15]. D. E. Barrick and E. Bahar, "Rough Surface Scattering Using Specular Point Theory," IEEE Trans. Antennas and Propagation, Vol. AP-29, No. 5, Sept., 1981, pp. 798-800.

[16]. W. Ellison (Marine Acoustics, Camb., Mass.), and in particular, more recently, by Gardiner Bishop (NUSC--Newport), at "Mini-Symposium on Sea-Ice Scattering Physics," organized by Dr. P. Cable NUSC--Code OIY, Sept. 25, 1984 at NUSC, New London, Conn.

[17]. E. Jahnke and F. Emde, Tables of Functions, G. E. Stechert, New York, 1938; pp. 6-9.

[18]. M. Abramowitz and I. A. Stegun, Handbook of Mathematical Functions, Nat'l. Bureau of Standards, Applied Mathematics Series, Vol. 55, U.S. Dept. of Commerce, U.S. Gov. Printing Office, Wash., D.C. 20402.

[19]. S. T. McDaniel and A. D. Gorman, "Examination of the Composite-Roughness Scattering Model," JASA 73, No. 5, May, 1983, pp. 1476-1486.

[20]. Reference [6], Sec. 11.2-2; esp. Eqs. (11.74), (11.75), extended to the spatial analogue of the time processes considered therein.

[21]. D. Middleton, "Multiple-Element Threshold Signal Detection of Underwater Acoustic Signals in Non-Gaussian Interference Environments," NOSC Contractor Report CR-231, May, 1984, prepared for Code 013, Naval Ocean Systems Center (NOSC), San Diego, Cal. 92152. See Sec. 7, Secs. 7.2, 7.3.

[22]. _____, "A Statistical Theory of Reverberation . . ., Part I," IEEE Trans. Information Theory, Vol. IT-13, No. 3, July, 1967, pp. 372-392, Section 2.

[23]. I. S. Gradshteyn and I. M. Ryzhik, Tables of Integrals, Products, and Series, Academic Press, New York, 1965.

[24]. Scientific and Engineering Studies--Underwater Acoustics in the Arctic, (Foreword, W. A. Von Winkle, Assoc. Tech. Director for Technology), Naval Underwater Systems Center, New London, Conn., Nov., 1984.

INITIAL DISTRIBUTION LIST

External	No. of Copies
ASN (RE&S)	1
OUSDR&E (Research & Advanced Technology)	2
Principal Dep Assist Secretary (Research	1
CNO, OP-02, -098, -21-T (Dr. E. Harper), -951E (CAPT M. J. Schneider)	4
NAVSEASYSCOM, -409-C (Dr. Snuggs), -63R (D. Porter), -63D (Dr. Y. Yam)	3
ONR, -425-AR (Dr. L. Johnson, Dr. R. Obrachta, Dr. M. McKisic, Dr. R. Fitzgerald), 411SP (Dr. N. Gerr), -410 (Dr. E. Wegman), -425 (Dr. Bradley)	7
NOSC (M. Morrison, J. Stewart, H. Bucker), 013 (Dr. E. Cooper) (3), 7133 (Dr. C. Persons), 5322 (Dr. J. Northrup), (Dr. F. Fisher, Dr. F. Speigs (Marine Physical Lab))	10
NORDA (R. Martin, R. Gardner, G. Gotthardt, E. Chaika, S. Chin-Bing, J. Posey, R. W. Farwell, W. Carey)	8
NRL (O. Diachock)	2
NISC, 23235 (E. Hansen)	1
SCRIPPS (Dr. W. Munk, Dr. F. Fisher)	2
ONT (Dr. T. Warfield, CAPT E. Young)	2
NROTC and NAU, MIT (CAPT David Burke)	1
Polar Research Laboratory (B. Buck)	1
APL/Univ of Wash (Dr. R. Francois)	1
Signatron (Dr. J. Pierce)	1
BB&N Inc. (Dr. H. Cox)	1
Operation Research, Inc. (Dr. V. Simmons)	1
Defense Systems, Inc. (G. S. Sebestyen)	1
Analysis and Technology, Inc. (Dr. P. Stocklin)	1
ITS/NTIA: U.S. Dept. of Commerce, (Dr. A. Spaulding, D. Crombie, Dr. C. Rush)	3
ARL, Univ of Texas, (Dr. G. Wilson, G. Ellis, Prof. C. Horton)	3
DTIC	2
NAVPGSCOL (Prof. Herman Medwin (1))	2
Science Applications Inc. (W. Chadsey, Dr. R. Becherer, Dr. G. Stegan, Dr. Tatros, M. J. Brackett Hersey, R. Green, J. Hanna)	7
ARL/PENN STATE, State College (Dr. S. McDaniel)	1
"Cyberlink," Boulder, CO (Dr. P. McManamon)	1
ARL, Johns Hopkins (Dr. J. Apel)	1
WPL-NOAA (Wave Propagation Lab) (Dr. D. Barrick)	1
Johns Hopkins Univ., Dept. of Oceanography (Prof O. Phillips)	1
Univ. of Wisconsin, Dpet. of Geophysics (Prof. C. Clay)	1
Univ. of New Mexico, Dept. of Elec. Eng. (Prof D. Petersen)	1
Univ. of Miami/RSMAS (Dr. F. Tappert)	1
Dr. David Middleton, New York, NY	10
PSI (Dr. R. Mellen)	1

END

FILMED

9-85

DTIC